

Open Cluster Members in the APOGEE DR17. I.

Dynamics and Star Members

R. Guerço^{1,2}, D. Souto³, J. G. Fernández-Trincado², S. Daflon¹, K. Cunha^{4,1}, J. V. Sales-Silva¹, V. Loaiza-Tacuri^{1,3}, V. V. Smith⁵, M. Ortigoza-Urdaneta⁶, and M. P. Roriz¹

¹ Observatório Nacional / MCTI, R. Gen. José Cristino, 77, 20921-400, Rio de Janeiro, Brazil

² Instituto de Astronomía, Universidad Católica del Norte, Av. Angamos 0610, Antofagasta, Chile
e-mail: rafael.fraga@ucn.cl, jose.fernandez@ucn.cl

³ Departamento de Física, Universidade Federal de Sergipe, Av. Marcelo Deda Chagas, S/N Cep 49.107-230, São Cristóvão, SE, Brazil

⁴ Steward Observatory, University of Arizona, 933 North Cherry Avenue, Tucson, AZ 85721-0065, USA

⁵ NSF's NOIRLab, 950 N. Cherry Ave. Tucson, AZ 85719, USA

⁶ Departamento de Matemática, Facultad de Ingeniería, Universidad de Atacama, Copiapó, Chile

Accepted June 17, 2025

ABSTRACT

Context. Open clusters are groups of stars formed from the same cloud of gas and cosmic dust. They play an important role in studying stars' formation and evolution and understanding galaxies' structure and dynamics.

Aims. The main objective of this work is to identify stars that belong to open clusters using astrometric data from Gaia EDR3 and spectroscopic data from APOGEE DR17. Furthermore, we investigate the metallicity gradients and orbital properties of the open clusters in our sample.

Methods. By applying the HDBSCAN clustering algorithm to this data, we identified observed stars in our galaxy with similar dynamics, chemical compositions, and ages. The orbits of the open clusters were also calculated using the GravPot16 code.

Results. We found 1987 stars belonging to 49 open clusters, and 941 of these stars have probabilities above 80 % of belonging to open clusters. Our metallicity gradient presents a two-slope shape for two measures of different Galactic center distances, the projected Galactocentric distance, and the guiding center radius to the Galactic Center, as already reported in previous work. However, when we separate the open clusters by age, we observe no significant difference in the metallicity gradient slope beyond a certain distance from the Galactic center. Our results show a shallower gradient for clusters younger than 2 Gyr than those older than 2 Gyr. All our OCs dynamically assemble the Disk-like population very well, and they are in prograde orbits, which is typical for disk-like populations. Some OCs resonate with the Galactic bar at the Lagrange points L4 and L5.

Key words. open clusters and associations: general – Methods: data analysis – Surveys – Galaxy: kinematics and dynamics

1. Introduction

Open Clusters (OCs) are composed of groups of stars that are believed to have formed from the same molecular cloud over a relatively short formation time, thus their stellar members share a nearly common age and chemical composition, making them excellent laboratories for studying stellar evolution. Milky Way open clusters are predominantly located along the Galactic plane (GP), with the youngest examples typically found within 100 pc of the GP. In contrast, older clusters can be located at Galactic altitudes greater than one kpc from the plane (Cantat-Gaudin & Casamiquela 2024). Due to their coeval nature and nearly identical chemistry, cluster members can be fit by stellar isochrones, resulting in distances that are relatively well constrained, and OC chemical abundances have played a pivotal role in probing chemical trends, such as abundance gradients, across the Galactic disk (Casamiquela et al. 2021). In ad-

dition to their relatively well-defined distances, the ages of OCs are also known and have been used to study chemical evolution or abundance gradients as functions of time. Recent advances in observational technology, including larger telescopes, multifiber spectrographs, and large high-resolution spectroscopic surveys, such as Gaia-ESO (Gilmore et al. 2012), GALAH (Martell et al. 2017), and APOGEE (Majewski et al. 2017), have significantly broadened our understanding of OCs, while the Gaia mission (Gaia Collaboration et al. 2016, 2018, 2021) has been fundamental in expanding the known census of OCs to nearly seven thousand clusters (Hunt & Reffert 2023). Maximizing the scientific return offered by OC stars requires, as a first step, identifying bona fide cluster members with minimal contamination from interloping field-star nonmembers. Techniques for determining stellar membership in clusters have advanced in recent years through the use of unsupervised machine learning methods, particularly density-based hierarchical algorithms, as illus-

trated by Castro-Ginard et al. (2018), Cantat-Gaudin & Anders (2020), and Castro-Ginard et al. (2022).

As reported by Randich et al. (2022), the Gaia-ESO Survey (GES) has concluded a decade-long effort by delivering a final spectroscopic catalogue comprising more than 100,000 stars, including advanced stellar parameters, chemical abundances, and cluster membership information. As the only extensive spectroscopic survey conducted with an 8m-class telescope to date, GES implemented a multi-pipeline analysis strategy and a refined homogenization procedure, establishing methodological standards now adopted by upcoming surveys such as WEAVE and 4MOST. The final data products, especially when combined with Gaia (e)DR3 and asteroseismic data, are expected to provide a long-term legacy for Galactic structure and evolution studies.

In the era of big data, machine learning has become crucial for obtaining valuable insights and making data-driven decisions. Machine learning refers to the ability of software to learn from data and improve autonomously from statistical algorithms without the need for explicit programming for each specific task. This field encompasses various techniques and algorithms designed to recognize patterns, make predictions, and efficiently classify data (Hopfield & Tank 1986). Within the broad scope of machine learning, clustering techniques play a key role in organizing datasets into homogeneous groups. Among the most advanced and flexible techniques in this domain is the Hierarchical Density-Based Spatial Clustering of Applications with Noise (HDBSCAN, Campello et al. 2013, 2015). HDBSCAN extends the widely-used Density-Based Spatial Clustering of Applications with Noise (DBSCAN, Ester et al. 1996) algorithm, enhancing its capacity to identify structures in high-density data and effectively manage noise. This enables the identification of data clusters of varying sizes and shapes without needing a prior specification of the number of clusters. In the works of Hunt & Reffert (2021, 2023); Chi et al. (2023); Loaiza-Tacuri et al. (2023); Grilo et al. (2024), HDBSCAN has shown its effectiveness in isolating high-probability stellar members of OCs.

The dynamical evolution of OCs is shaped by tidal forces from the Galactic disk and molecular clouds (Friel 1995). Theoretical models predict that OCs generally dissolve within 10^8 to 10^9 years, with disruption timescales depending on mass and core radius (Spitzer 1958; Spitzer & Harm 1958). Only the most massive and centrally concentrated clusters, or those in less disruptive orbits, tend to survive (Friel 1995). The motion and spatial distribution of Galactic OCs provide valuable insight into the gravitational potential and perturbations that influence the structure and dynamics of the Milky Way (Soubiran et al. 2018). Computational tools have been developed to model the Galactic gravitational potential and therefore study its dynamics: NEMO (Teuben 1995), GalPot (Dehnen & Binney 1998; McMillan 2017b,a), galpy (Bovy 2015), GravPot16 (Fernández-Trincado 2017) and AGAMA (Vasiliev 2019). This work uses the GravPot16 code, a tool designed for Galactic dynamics and orbit integration, whose steady-state gravitational potential has been inferred from the superposition of the multiple galactic components of the popular Besançon galaxy model (Robin et al. 2003, 2012, 2014). It allows for detailed simulations of the OC dynamics, providing insights into their past trajectories and future evolution. By integrating observational data with sophisticated models such as GravPot16, researchers can reconstruct the orbits of OCs (Schiappacasse-Ulloa et al. 2018), assess their interactions with Galactic structures, and assess their susceptibility to disruption.

This paper is organized as follows: the methodology for obtaining OC stellar members that were observed spectroscopically by the APOGEE survey is presented in Section 2. The OC members identified here and their cluster membership probabilities are compared with those from other studies in Section 3. Section 4 provides a discussion of the dynamics of the APOGEE OC sample, along with the metallicity (as [Fe/H]) gradients derived from these clusters. Conclusions are then presented in Section 5.

2. Methodology and sample

2.1. HDBSCAN

We apply the HDBSCAN machine learning algorithm to a sample of stars observed by Gaia and the APOGEE survey to identify stars with similar dynamics, chemical compositions, and ages in our Galaxy, specifically those belonging to open clusters. HDBSCAN builds on DBSCAN by using the minimum number of points (m_{Pts}) parameter to define core and border points and introduces the minimum cluster size (m_{cSize}) parameter, which sets the minimum number of data points needed to form a cluster. Fine-tuning the m_{cSize} parameter is crucial in optimizing HDBSCAN's performance, as it depends on the dataset's characteristics. A larger m_{cSize} leads to fewer and larger clusters, potentially merging smaller, denser clusters into larger ones. In contrast, a smaller m_{cSize} identifies smaller, denser clusters but may also result in more noise being classified as small clusters. The HDBSCAN hierarchy reflects clusters that appear and merge at multiple density levels. The stability of clusters is the key metric for the selection of clusters, with broad bases and sharp density peaks considered the most meaningful. This hierarchical approach makes HDBSCAN ideal for complex datasets, such as stellar populations, where structures at different density levels can exist.

We adopt the same values for m_{Pts} and m_{cSize} as recommended by Campello et al. (2013). Using equal values for m_{Pts} and m_{cSize} ensures consistency between the density definition and cluster size threshold in HDBSCAN. This approach avoids introducing biases by keeping the clustering process uniform and interpretable since the minimum cluster size directly aligns with the density required to form a cluster. It also simplifies parameter tuning while maintaining robust results, especially when working with datasets where clusters of varying densities coexist, fostering a more reliable identification of meaningful structures in the data. In Figure 1, we present the HDBSCAN cluster tree for two open clusters confirmed in this work: Berkeley 18 and M67, top and bottom panels, respectively. The cluster tree visually represents the hierarchical structure of the sample, illustrating how the clusters are nested within each other and how they merge as the distance threshold increases. The λ value in Figure 1 is the inverse of the core distance, where the core distance is defined as the distance to the k^{th} nearest neighbor, with k being a user-specified parameter. Higher values of λ correspond to higher density levels (more densely packed points). The height of a branch in the cluster tree (measured by λ) reflects the density level at which clusters merge or split. A higher branch height indicates that the cluster remains stable at higher densities, and clusters that persist over a wide range of λ values (have long branches) are considered more stable and robust. When moving up the tree (increasing λ), we see how smaller clusters merge into larger ones, indicating a hierarchical structure. The value of λ helps to identify the most stable clusters; by examining the range of λ over which a cluster exists, one can determine its persistence and robustness. Clusters with high λ stability scores are

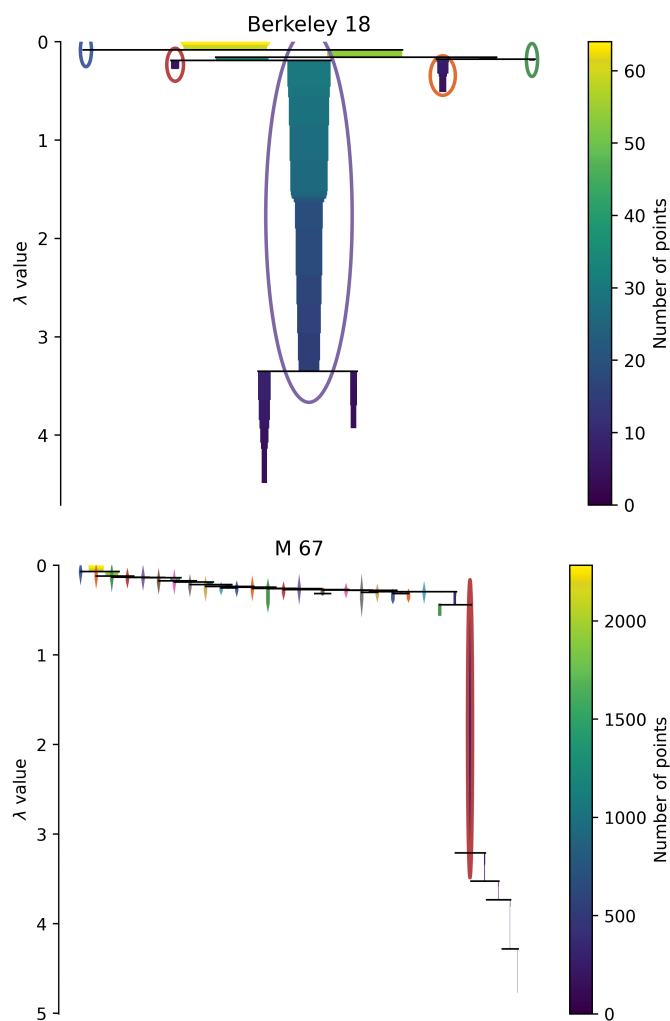


Fig. 1: The cluster tree, or dendrogram, produced by HDBSCAN code. The λ value is equal to the inverse of the core distance, being a measure related to the density-based nature of the HDBSCAN, and helps in understanding the hierarchy and persistence of clusters.

considered meaningful. Points or clusters with shallow λ values are often considered noise or outliers since they only exist at low-density levels. We can then assume that the branches with greater values of λ in Figure 1 represent the members of the OCs Berkeley 18 (top panel) and M 67 (bottom panel).

2.2. Sample

Our analysis is based on the final results of SDSS-IV APOGEE DR17, as reported by Abdurro'uf et al. (2022). APOGEE spectra are obtained using two cryogenic, multi-fiber spectrographs (with 300 fibers) that observe in the near-infrared H-band, covering wavelengths from 1.51 to 1.69 μm (Gunn et al. 2006; Wilson et al. 2010, 2019). These spectrographs are located in the Northern and Southern hemispheres: one at Apache Point Observatory (APO) in New Mexico, USA, and the other at Las Campanas Observatory (LCO) near La Serena, Chile. The main objective of the APOGEE survey was to determine the chemical composition and kinematics of red giant stars to study the chemical evolution and dynamics of stellar populations in the Milky

Way. A large number of open cluster stars were observed and analyzed as part of this effort.

The APOGEE DR17 dataset contains more than 657,000 stars, with stellar parameters and chemical compositions derived from high-resolution spectra ($R \approx 22,500$). Radial velocities and metallicities for all stars were automatically determined by the APOGEE pipeline (Nidever et al. 2015; García Pérez et al. 2016), with typical uncertainties of $1.0 \text{ km}\cdot\text{s}^{-1}$ for radial velocity and approximately 0.02 dex for metallicity.

3. Membership analysis from HDBSCAN

As a first step, we selected OCs from DR17 based on the RA and DEC of their centers as given in previous studies (Donor et al. 2020, OCCAM; Cantat-Gaudin & Anders 2020; Hunt & Reffert 2023). We applied filters to these data to ensure quality, including removing possible binaries from the sample. The APOGEE VSCATTER parameter, which measures the variation in radial velocity (RV) in multiple observations, was used as an indicator of binarity, with a cutoff threshold of $1 \text{ km}\cdot\text{s}^{-1}$, a typical value adopted by other studies (Bailer-Jones et al. 2021; Quispe-Huaynasi et al. 2022), and validated, for example, by Jönsson et al. (2020).

The following parameters were used as input for HDBSCAN in our analysis: right ascension (RA), declination (DEC), parallax (π), proper motions (μ_{RA} and μ_{DEC}), radial velocity (RV), and metallicity ($[\text{Fe}/\text{H}]$). The parameters RA, DEC, π , μ_{RA} , and μ_{DEC} are sourced from the Gaia EDR3 data (Gaia Collaboration et al. 2021), while RV and $[\text{Fe}/\text{H}]$ are taken from the APOGEE DR17 data set (Abdurro'uf et al. 2022). The region selected to be considered in the HDBSCAN analysis for each OC was determined using the cluster center. From the center of each OC, we define the ratio between the window size in RA or DEC ($\delta(\text{RA})$ and $\delta(\text{DEC})$) and the GAIA DR3 parallax of each OC as 6. This ratio was empirically chosen and has been well suited to improve our membership analysis. Nonetheless, in a few cases, we considered this ratio with values different from 6: Berkeley 98 (ratio 8), and Berkeley 19, Berkeley 33, King 8 (ratio 10), for better operation of the HDBSCAN code.

3.1. Cluster membership

We identified 1,987 stars across 49 open clusters, with 1,456 stars having a membership probability above 50% and 941 stars with a probability above 80%. These results are presented in Tables A.1 and B.1. HDBSCAN assigns a membership probability to each star by evaluating its proximity to the densest regions of the OC across the combined dimensions. Stars that exhibit consistent spatial location, velocity, and chemical composition with the core members receive higher probabilities (close to 1). Conversely, stars that deviate in one or more parameters receive lower probabilities, reflecting their possible outlier or transition status. This approach ensures a robust classification of the OC membership by accounting for kinematic and metallicity coherence among stars.

We run HDBSCAN iteratively, varying m_{clsize} from 2 to 10, and computed the mean and standard deviation of the input parameters for each run. The optimal m_{clsize} value for each open cluster was determined by selecting the value that led to the smallest standard deviation of the mean metallicity of stars with membership probabilities greater than 80%. This assumes, of course, that open clusters have homogeneous chemical abundances. We note that in cases where the standard deviation was

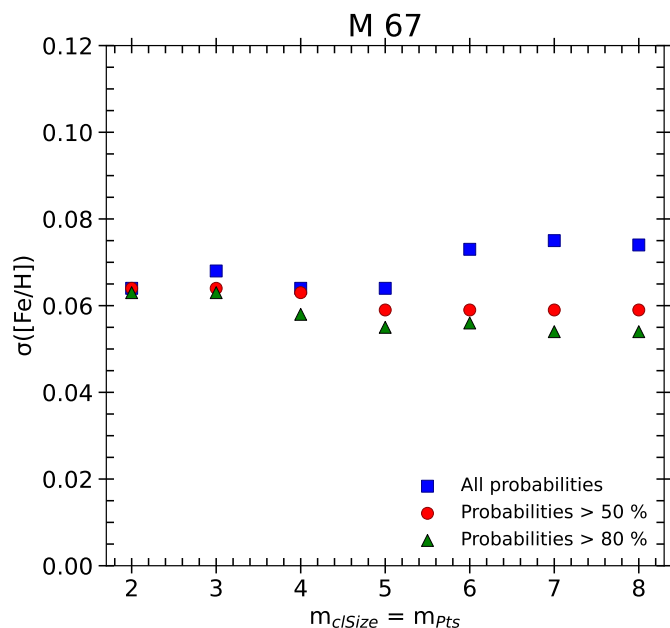


Fig. 2: m_{clSize} vs. $\sigma([Fe/H])$ of M 67. The blue squares represent all stars, the red circles represent the stars with probabilities greater than 50 %, and the green triangles represent the stars with probabilities greater than 80 %.

approximately equal for multiple m_{clSize} values, we used the smallest standard deviation from the metallicities including all stars from the OC group selected by HDBSCAN.

Figure 2 illustrates how m_{clSize} was selected for the open cluster M 67. For each m_{clSize} , the standard deviation of the mean metallicity ($\sigma([Fe/H])$) was calculated for all stars (blue squares), stars with probabilities greater than 50% (red circles), and stars with probabilities greater than 80% (green triangles). In the case of M 67, we selected $m_{clSize} = 5$, as it resulted in one of the lowest $\sigma([Fe/H])$ for stars with membership probabilities greater than 80%. In this case, we do not consider $m_{clSize} = 7$, with $\sigma([Fe/H])$ approximately equal to $m_{clSize} = 5$ for stars with membership probabilities greater than 80%, because the $\sigma([Fe/H])$ for all stars (blue squares) is much greater than $\sigma([Fe/H])$ obtained with $m_{clSize} = 5$. The m_{clSize} values for all 49 open clusters analyzed in this study are provided in Table B.1.

The HDBSCAN clustering result for M 67 is shown in the top panel of Figure 3. We chose a search window for M67 members with 2283 stars (gray circles) centered on the central cluster position obtained in Donor et al. (2020), Cantat-Gaudin & Anders (2020), and Hunt & Reffert (2023). The stars selected as members are represented with blue circles, whose sizes represent the probability of belonging to the OC (378 stars for M 67). The number of stars (N_{all}) obtained for each cluster is shown in Table B.1.

3.2. Comparison with previous studies

The lower panels of Figure 3 show the cross-match of our results with Hunt & Reffert (2023) (red triangles in the lower left panel) and Cantat-Gaudin & Anders (2020) (red triangles in the lower right panel) for M67 stars. In this figure, we show only stars with probabilities above 80 % from Hunt & Reffert (2023) and Cantat-Gaudin & Anders (2020). In this example, we iden-

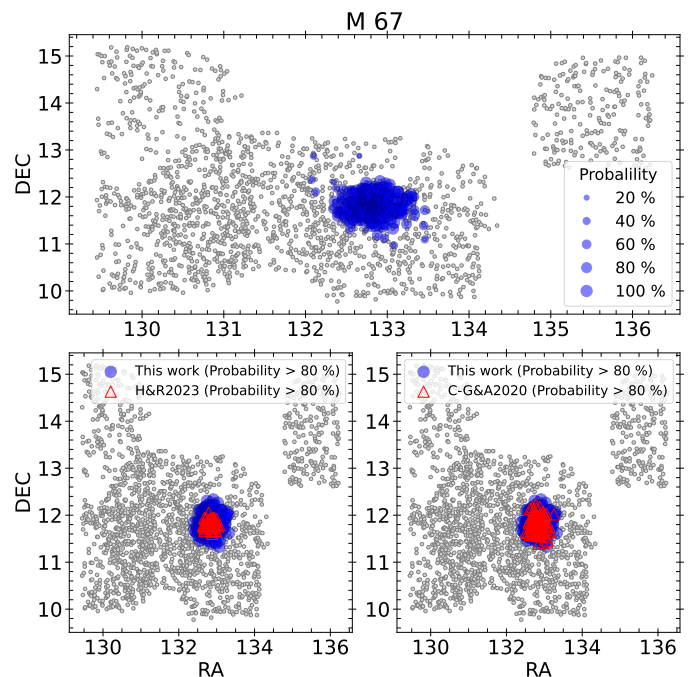


Fig. 3: Window Right Ascension (RA) vs. Declination (DEC) centered on the position of M 67 by Donor et al. (2020), Cantat-Gaudin & Anders (2020) and Hunt & Reffert (2023). The gray circles are the stars used in HDBSCAN to search for members of M 67. The blue circles are the members obtained with the HDBSCAN code. In the upper panel, the caption indicates the probability of each star belonging to the OC according to the size of the blue circle. Lower left panel: The blue circles represent our results for stars with a probability of belonging to the OC greater than 80 %. In contrast, the red triangles represent the results of Hunt & Reffert (2023) with probabilities belonging to the OC above 80 %. Lower right panel: The blue circles represent our results for stars with a probability of belonging to the OC greater than 80 %, while the red triangles represent the results of Cantat-Gaudin & Anders (2020) with probabilities of belonging to the OC above 80 %.

tified 257 stars with probabilities greater than 80 % of belonging to M 67. Compared with the same probability range ($P > 80\%$), we have 84 stars in common with Hunt & Reffert (2023) and 146 stars in common with Cantat-Gaudin & Anders (2020). For NGC 2158, for example, we have 27 stars in common with Hunt & Reffert (2023) and 54 stars in common with Cantat-Gaudin & Anders (2020), for stars with probabilities greater than 80 % to be members of the cluster.

A comparison of our membership results with Hunt & Reffert (2023), which employed the HDBSCAN code using the astrometric parameters from GAIA DR3 of RA, DEC, μ_{RA} , μ_{DEC} and π as input parameters, finds that we have more stars classified by HDBSCAN as members with probabilities above 80 % when compared with Hunt & Reffert (2023). The probable explanation for this is illustrated in Figure 4, which compares our membership probabilities with those from Hunt & Reffert (2023) for M 67 (top panel) and Berkeley 18 (lower panel) stars, with the colors showing the individual stellar radial-velocity standard deviations (σ) from the mean cluster RV: green represents 0σ to 1σ , blue represents 1σ to 2σ , and red represents 2σ to 3σ . Our membership probability

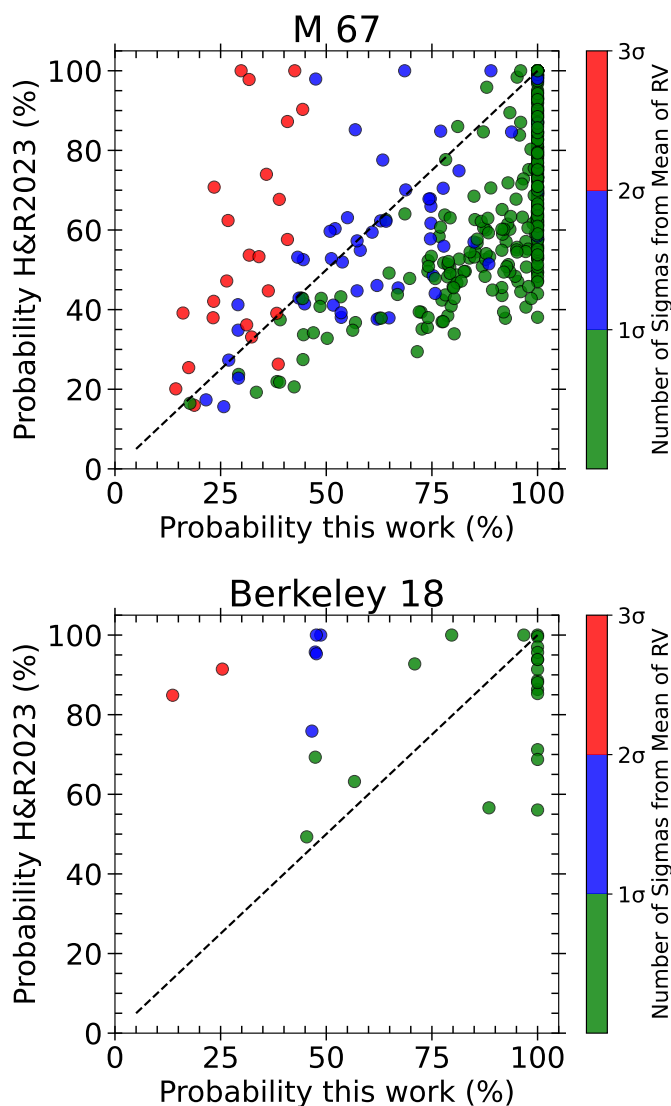


Fig. 4: Probabilities from this work versus probabilities from Hunt & Reffert (2023) (H&R2023) for M 67 (top panel) and Berkeley 18 (lower panel) stars. The color bar shows the number of standard deviations (σ) from the cluster RV mean: green represents deviation $\leq 1\sigma$, blue represents between 1σ and 2σ and red represents between 2σ and 3σ .

is thus weighted by RV, as we have adopted this as an input parameter, unlike the analysis of Hunt & Reffert (2023).

Regarding metallicities, we find that open clusters exhibit [Fe/H] values with low σ for their stars that have probabilities greater than 80%. For the 49 OCs included here, the typical value of σ ([Fe/H]) ~ 0.04 dex, using the [Fe/H] values from DR17. These standard deviations were used as a criterion in HDBSCAN to determine the value of $m_{c\text{size}}$ for each OC (see Table B.1). Furthermore, Figure 4 highlights the importance of including RV as a criterion to enhance confidence in stars classified with probabilities of being OC members in Hunt & Reffert (2023). Stars with RV values closer to the cluster average tend to show higher membership probabilities, with many achieving 100%. This pattern is also consistently observed in other OCs. For example, stars with RV standard deviations between 2σ and 3σ have probabilities below 50% of being M 67 members (top panel of Figure 4) or Berkeley 18 members (bottom panel of

Figure 4). These low σ values obtained align with recent works on open cluster homogeneity using the APOGEE spectra, such as Bovy (2016); Sinha et al. (2024). The authors find limits on open cluster homogeneity within 0.02 dex or less for most elements.

4. Discussion

4.1. Orbital elements of selected OCs

We used the state-of-the-art Milky Way model GravPot16¹ to predict the orbital path of OCs from our sample in a steady-state gravitational Galactic model that includes a “boxy/peanut” bar structure (Fernández-Trincado et al. 2019). This Galactic model is fundamental for predicting the structural and dynamic parameters of the Galaxy to the best of our recent knowledge of the Milky Way. We adopted the same model configuration, solar position, and velocity vector as described in Fernández-Trincado et al. (2019) for the orbit computations, except for the angular velocity of the bar (Ω_{bar}), for which we used the recommended value of $41 \text{ km s}^{-1} \text{ kpc}^{-1}$ (Sanders et al. 2019), and assuming variations of $\pm 10 \text{ km s}^{-1} \text{ kpc}^{-1}$. These structural parameters for our bar model (e.g., mass and orientation) are within observational estimations that lie in the range of $1.1 \times 10^{10} M_{\odot}$ and present-day orientation of 20° (value adopted from dynamical constraints, as highlighted in fig. 12 of Tang et al. 2018) in the non-inertial frame (where the bar is at rest). The lengths of the bar scale are $x_0 = 1.46 \text{ kpc}$, $y_0 = 0.49 \text{ kpc}$, and $z_0 = 0.39 \text{ kpc}$, and the middle region ends on the effective semi-major axis of the bar at $R_c = 3.28 \text{ kpc}$ (Robin et al. 2012).

For guidance, the Galactic convention adopted in this work is: X -axis is oriented toward $l = 0^{\circ}$ and $b = 0^{\circ}$, Y -axis is oriented toward $l = 90^{\circ}$ and $b = 0^{\circ}$, and the disc rotates toward $l = 90^{\circ}$; the velocity is also oriented in these directions. Following this convention, the Sun’s orbital velocity vectors are $[U_{\odot}, V_{\odot}, W_{\odot}] = [11.1, 12.24, 7.25] \text{ km s}^{-1}$, respectively (Schönrich et al. 2010). The model has been rescaled to the Sun’s Galactocentric distance, 8.27 kpc (GRAVITY Collaboration et al. 2021), and a circular velocity at the solar position of $\sim 229 \text{ km s}^{-1}$ (Eilers et al. 2019).

The most likely orbital parameters and their uncertainties are estimated using a simple Monte Carlo scheme. An ensemble of a half million orbits was computed backward in time for 2 Gyr, under variations of the observational parameters assuming a normal distribution for the uncertainties of the input parameters (e.g., positions, heliocentric distances, radial velocities, and proper motions), which were propagated as 1σ variations in a Gaussian Monte Carlo resampling. To compute the orbits, we adopt a mean RV (Table B.1) of the member stars computed from the APOGEE DR17 data (Abdurro’uf et al. 2022). The nominal proper motions ($\langle \mu_{RA} \rangle$ and $\langle \mu_{DEC} \rangle$ from Table B.1) for each cluster were taken from Gaia EDR3 (Gaia Collaboration et al. 2021), with an assumed uncertainty of 0.5 mas yr^{-1} for the orbit computations. Heliocentric distances (d_{\odot}) were adopted from Bailer-Jones et al. (2021). The results for the main orbital elements are listed in Table B.2.

Figure 5 shows a scatter plot of all possible combinations among the orbital elements in the non-axisymmetric model. In the same figure, we use three different angular velocities for the Galactic bar that are plotted with different colors and symbols in panels (b), (c), and (d). All selected clusters share the same kinematical behavior as the disk population, as illustrated in figure

¹ <https://gravpot.utinam.cnrs.fr>

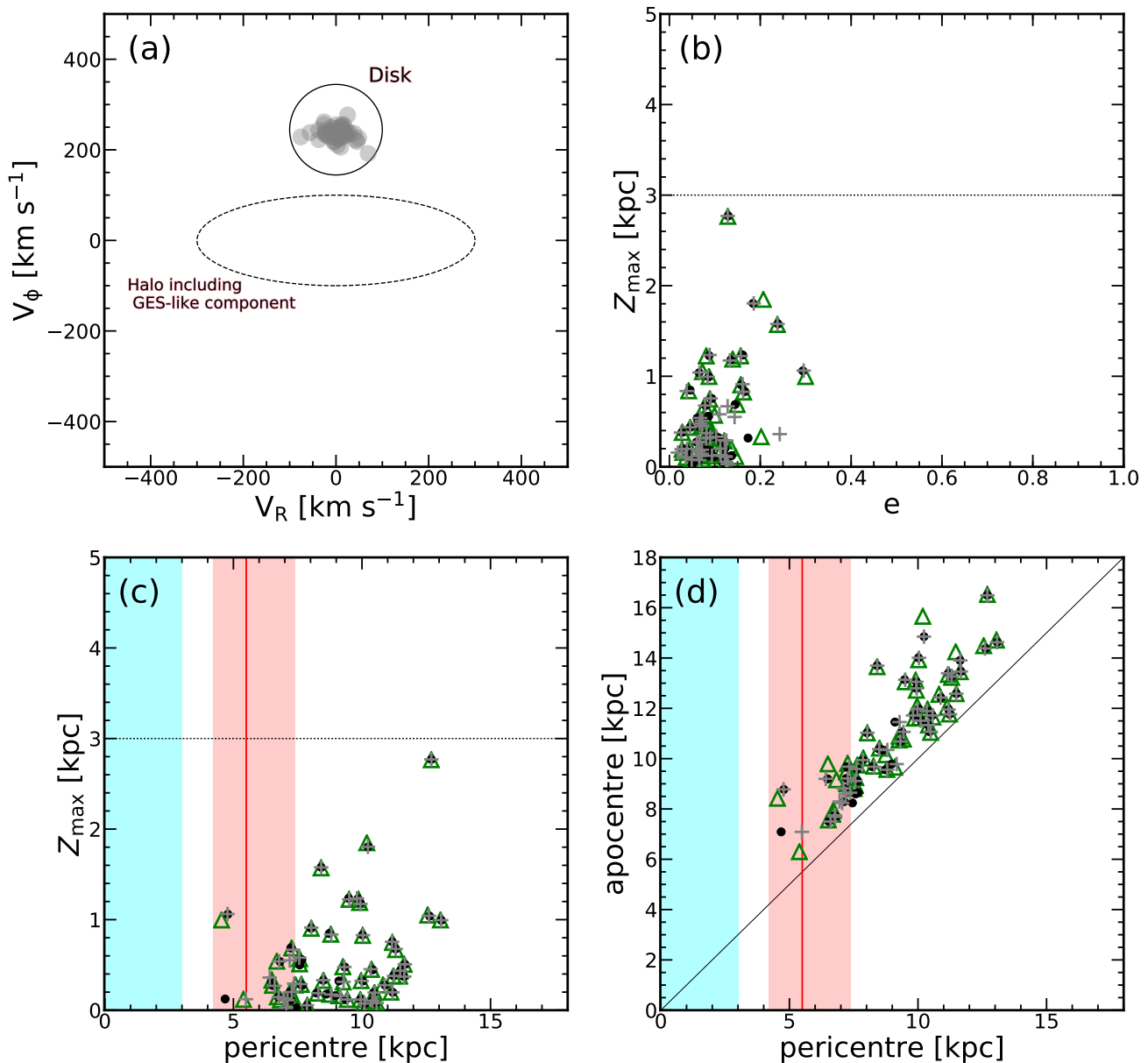


Fig. 5: Kinematics and orbital elements of selected OCs. In panel (a), the Galactocentric radial velocity (V_R) versus azimuthal velocity (V_ϕ) is shown for 49 selected OCs (grey symbols) which fall within the area occupied by the disk population (black circle). For guidance, a black dashed ellipsoid also highlights the halo *Gaia-Enceladus-Sausage*-like (Belokurov et al. 2018) area in the same panel. The remaining panels show the orbital elements by assuming $\Omega_{\text{bar}} = 31$ (green empty symbols), 41 (black symbols), and 51 (grey crosses) $\text{km s}^{-1} \text{kpc}^{-1}$. In panels (b,c) and (c,d) the black horizontal dotted line indicates a distance of ~ 3 kpc (i.e., the edge Z_{\max} of the thick disc; Carollo et al. 2010); while the cyan and red shaded region indicate the radius (i.e. 3 kpcs; Barbuy et al. 2018) of the Milky Way bulge, and location of the bar’s corotation radius (CR) between 4.2 kpcs ($\Omega_{\text{bar}} = 51 \text{ km s}^{-1} \text{kpc}^{-1}$) and 7.4 kpcs ($\Omega_{\text{bar}} = 31 \text{ km s}^{-1} \text{kpc}^{-1}$) with the red thick vertical line indicating the position of 5.5 kpc for $\Omega_{\text{bar}} = 41 \text{ km s}^{-1} \text{kpc}^{-1}$. The straight line in panel (d) shows the one-to-one line, which indicates that a cluster on this line would have a circular orbit.

5-(a). Orbital elements reveal that most clusters have low vertical excursions ($Z_{\max} < 2$ kpc) from the Galactic plane, except for Berkeley 20 (among the old clusters in our sample) that reach distances ($\sim 2.76 \pm 0.84$ kpc) closest to the edge $Z_{\max} \sim 3$ kpc of the thick disc (e.g., Carollo et al. 2010). It is not surprising that Berkeley 20 exhibits such high excursions in the Galactic plane, as we know that this cluster belongs to the old OCs in this sam-

ple, i.e., most of the old ($\text{AGE} > \log_{10}(8.6)$ Gyr) OCs in our sample exhibit a large scatter (~ 2 kpc) in Z_{\max} with vertical excursions from the Galactic plane $Z_{\max} > 0.2$ kpc. In comparison, young ($\text{AGE} < \log_{10}(8.6)$ Gyr) OCs are confined to less than ~ 0.2 kpc within the Galactic plane. For eccentricity, all clusters show low eccentricities, $e < 0.3$, and are characterized by pro-grade orbits relative to the direction of Galactic rotation.

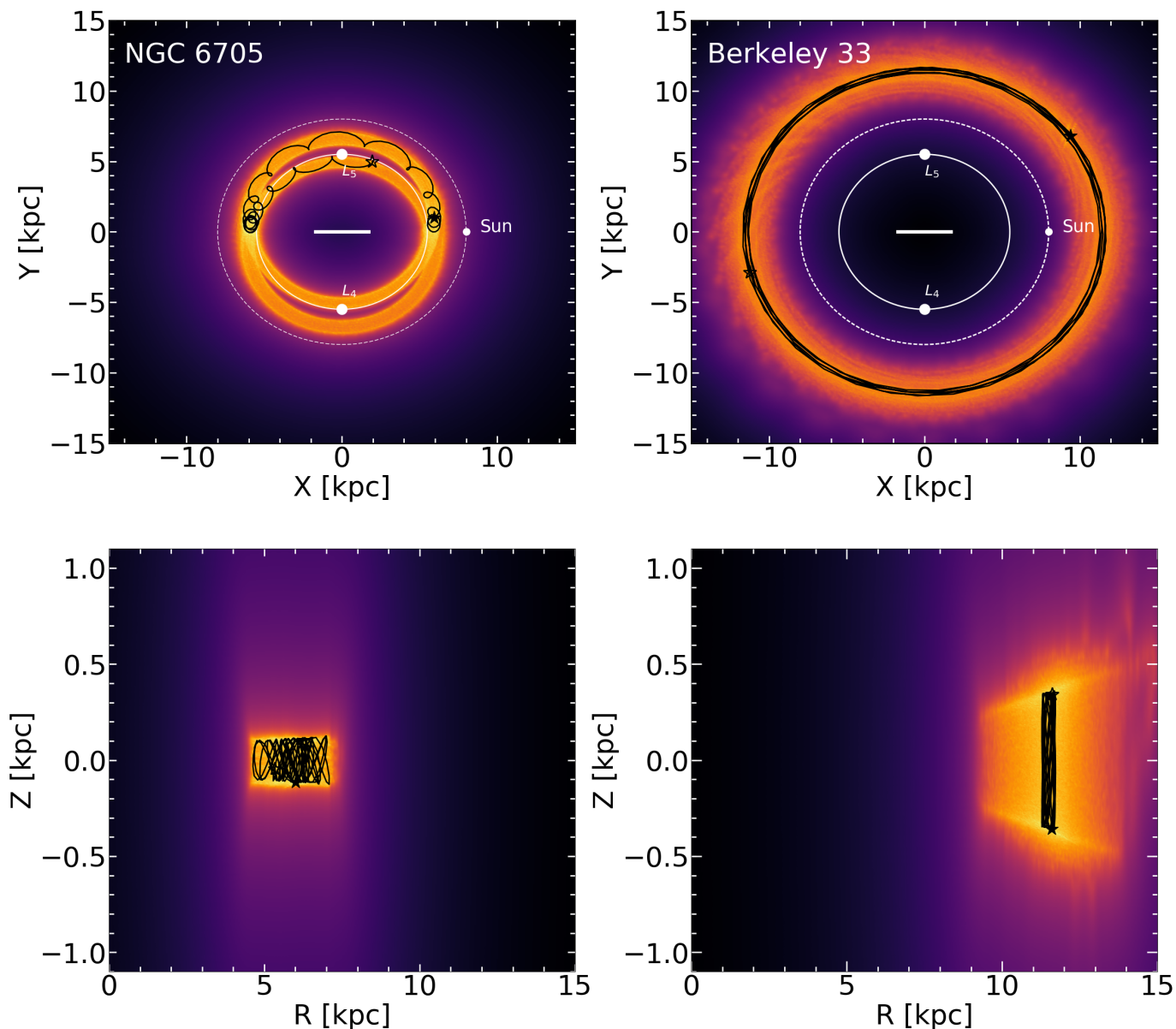


Fig. 6: Ensemble of half million orbits in the frame corotating with the bar for two selected OCs, projected on the equatorial (top) and meridional (bottom) Galactic planes in the non-inertial reference frame with a bar pattern speed of $41 \text{ km s}^{-1} \text{ kpc}^{-1}$, and time-integrated backward over 2 Gyr. The yellow and orange colors correspond to more probable regions of the space, which are most frequently crossed by the simulated orbits. The white inner solid and outer dashed circles in top panels show the locations of the CR and Solar orbit, respectively, while the white dots mark the positions of the Lagrange points of the Galactic bar, L_4 and L_5 , and the current Sun's position, respectively. The horizontal white solid line shows the extension of the bar ($R_c \sim 3.4 \text{ kpc}$; Robin et al. 2012) in our model. The black solid line shows the orbits of the selected OCs from the observables without error bars. The black-filled and unfilled star symbols indicate the initial and final positions of the OCs in our simulations, respectively.

Figure 6 shows two selected examples of the simulated orbits by adopting a simple Monte Carlo approach. The probability densities of the resulting orbits projected on the equatorial and meridional galactic planes in the non-inertial reference frame, where the bar is at rest, are highlighted in the same figure. The black line in the figure shows the orbital path (adopting observables without uncertainties). At the same time, yellow corresponds to more probable regions of space that are crossed more frequently by the simulated orbits. It is interesting to note that some particular cases shown in Figure 6, such as NGC 6705,

exhibit a chaotic orbital configuration that has a banana-shaped shape parallel to the bar, which circulates the Lagrange points L_4 and L_5 , with orbits that move around CR, but eventually become trapped by the Lagrange point L_4 or L_5 . This is unusual dynamical behavior for bar-induced OCs and is likely related to some moving groups, such as the so-called Hercules stream (Pérez-Villegas et al. 2017). Our results could provide insight into the formation processes and origin of the moving groups in the solar neighborhood.

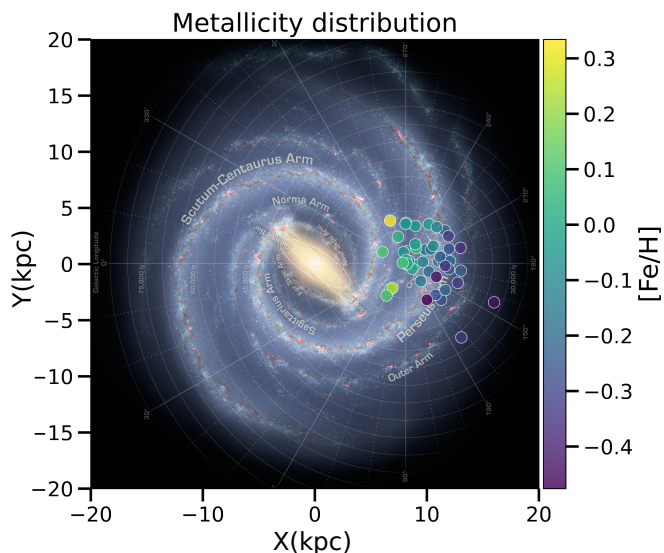


Fig. 7: Distributions in Galactocentric coordinations X and Y of the 49 OCs. The color bar represents the metallicity between -0.48 and 0.33 dex. We use the `mw-plot` <https://milkyway-plot.readthedocs.io>

Additionally, a compilation of simulated orbital projections on the equatorial Galactic planes in the non-inertial reference frame with a bar pattern speed of $31 \text{ km s}^{-1} \text{ kpc}^{-1}$, $41 \text{ km s}^{-1} \text{ kpc}^{-1}$ and $51 \text{ km s}^{-1} \text{ kpc}^{-1}$ are shown in the Appendix in Figures C.1, D.1, and E.1, respectively. The orbits shown in these figures have been simulated by adopting the observable radial velocity, heliocentric distance, and proper motions without error bars. A few OCs in disk-like orbits show oscillations in/out of the corotation radius, meaning these OCs are trapped in resonance with the bar and moving around some of the Lagrange points. In other words, these few OCs are likely describing chaotic orbits. However, there is a strong dependence on the bar angular velocity, Ω_{bar} , demonstrating that including a Galactic bar is important to describe the dynamical history of the OCs in the Galaxy.

4.2. Metallicity gradients

Figure 7 presents the distribution of the 49 OCs studied in Galactocentric coordinates X and Y (Table B.2). Values of $[\text{Fe}/\text{H}]$ (Table B.1) are represented by the color bar spanning the interval between -0.48 and $+0.33$ dex. We used the `mw-plot`² code to obtain the Milk Way map that is modified from an image by NASA/JPL-Caltech/R. Hurt (SSC/Caltech). The clusters occupy distances from the Galactic center between 6.14 and 16.36 kpc, displaying the well-known anti-correlation between metallicity and the Galactocentric distance. This figure shows that clusters roughly between the Centaurus and Perseus arms have metallicities between $+0.0$ and $+0.3$ dex, while clusters along the Perseus arm display metallicities varying from -0.4 to $+0.0$ dex. In particular, the two more distant clusters, Tombaugh 2 and Berkeley 20, exhibit lower metallicities ($[\text{Fe}/\text{H}] = -0.35$ and -0.44 dex, respectively).

Figure 8 shows the metallicity gradients as functions of the projected Galactocentric distance (R_{GC} , left panels) and the guiding center radius (R_{Guide} , right panels), whose values are presented in Table B.2. In panels (a) and (b), the red curves

represent the median $[\text{Fe}/\text{H}]$ for each 1.5 kpc bin within the interval range from $6 - 16.5$ kpc (panel a) and the range $6 - 15$ kpc (panel b), while the pink strip represents the median absolute deviation (MAD) of $[\text{Fe}/\text{H}]$. In panels (c) and (d) of Figure 8, two linear regressions are shown for each panel.³ We compare our results with those of Spina et al. (2022) (purple lines in panel c), Myers et al. (2022) (orange lines in panels c and d) and Magrini et al. (2023) (green lines in panel c). As found by Spina et al. (2022), Myers et al. (2022) and Magrini et al. (2023), our linear fits show a pronounced decrease in $[\text{Fe}/\text{H}]$ with R_{GC} and R_{Guide} for R_{GC} between $6.0-11.5$ kpc ($d[\text{Fe}/\text{H}]/dR_{GC} = -0.085 \pm 0.011 \text{ dex/kpc}$) and R_{Guide} between $6.0-10.5$ kpc ($d[\text{Fe}/\text{H}]/dR_{Guide} = -0.090 \pm 0.005 \text{ dex/kpc}$). In panel (c), the clusters farthest from the Galactic center (R_{GC} between $11.5-16.5$ kpc) follow a shallower slope, with the same value as found by Myers et al. (2022), with $d[\text{Fe}/\text{H}]/dR_{GC} = -0.032 \text{ dex/kpc}$, while Magrini et al. (2023) finds a slightly steeper slope ($d[\text{Fe}/\text{H}]/dR_{GC} = -0.044 \text{ dex/kpc}$), but still within our respective uncertainties. In panel (d) of Figure 8, we found a difference in the cutoff R_{Guide} between the two groups of OCs with different slopes compared to Myers et al. (2022). The inner and outer gradients of Myers et al. (2022) have the cutoff $R_{Guide} = 12.2$ kpc, while in this work, the cutoff R_{Guide} is 10.5 kpc.

Panels (e) and (f) from Figure 8 show three linear regressions for three age intervals within the 49 OCs (Cantat-Gaudin & Anders 2020 ages; Table B.1), which were also used by Myers et al. (2022), with ages from 0.02 to 4.00 Gyr: 17 OCs have ages less than 1 Gyr (green circles), 13 OCs have ages between 1 and 2 Gyr (red circles), and 19 OCs have ages greater than 2 Gyr (orange circles). Using this age separation, we can see that the groups of OCs represented by the green and red circles have only small differences in their gradients with R_{GC} ($d[\text{Fe}/\text{H}]/dR_{GC} = -0.067 \pm 0.004$ and $-0.066 \pm 0.004 \text{ dex/kpc}$, respectively), and R_{Guide} ($d[\text{Fe}/\text{H}]/dR_{Guide} = -0.070 \pm 0.003$ and $-0.065 \pm 0.006 \text{ dex/kpc}$, respectively). Meanwhile, clusters older than 2 Gyr show significantly steeper slopes, with $d[\text{Fe}/\text{H}]/dR_{GC} = -0.074 \pm 0.018 \text{ dex/kpc}$ and $d[\text{Fe}/\text{H}]/dR_{Guide} = -0.088 \pm 0.010 \text{ dex/kpc}$, as represented by the orange lines in panels (e) and (f). Carraro et al. (1998); Friel et al. (2002); Chen et al. (2003); Magrini et al. (2009); Netopil et al. (2022); Magrini et al. (2023) also found this trend of a steeper decrease in metallicity for older OCs as they fall further from the Galactic center. In this work, it is clear that there is no break in the metallicity gradient when we consider only OCs with ages less than 2 Gyr (black lines in g and h panels) with $d[\text{Fe}/\text{H}]/dR_{GC} = -0.066 \pm 0.004 \text{ dex/kpc}$ and $d[\text{Fe}/\text{H}]/dR_{Guide} = -0.067 \pm 0.005 \text{ dex/kpc}$; and ages higher than 2 Gyr (panels g and h are the same as the e and f panels).

Unlike the works of Magrini et al. (2023) and Palla et al. (2024), our sample of the youngest OCs (ages < 1 Gyr) located in the inner Galaxy does not exhibit such a pronounced difference in metallicity when compared to older OCs. Magrini et al. (2023) found that the metallicities of young OCs are significantly lower than those of older OCs in the inner Galaxy. Based on these results, Palla et al. (2024) proposed that a late episode of gas accretion, triggering a metal dilution – a scenario previously suggested by Spitoni et al. (2023) for the solar neighborhood – may be responsible for this difference. However, our results do not indicate such a marked metallicity difference between young and old OCs in the inner Galaxy.

³ The lines (linear regressions) from this work in the panels (c), (d), (e), (f), (g), and (h) of Figure 8 were determined with the `sklearn.linear_model` package in Python.

² <https://milkyway-plot.readthedocs.io>

The steeper metallicity gradients for older OCs compared to younger ones can be understood in terms of the formation and evolution of the Galactic disk. As stars form and evolve in the disk, they incorporate heavier elements, or metals, which are enriched through processes such as stellar nucleosynthesis and supernova explosions. This enrichment process and Galactic dynamics influence metallicity distribution across the disk (Matteucci 2021). For the old OCs, the metallicity gradient steepens due to the differing rates of star formation and chemical enrichment in different regions of the Galactic disk. Younger clusters, on the other hand, may have formed in a more homogeneous environment, leading to a shallower gradient. Studies such as those by Magrini et al. (2023) and Netopil et al. (2022) show that metallicity gradients are steeper for older clusters, particularly as they move away from the Galactic center. The combination of longer star formation histories, galactic dynamics, and enrichment processes explains why older open clusters exhibit a stronger metallicity gradient than their younger counterparts.

Our metallicity gradient results (Figure 8) are consistent with those obtained by Myers et al. (2022), who found that the OCs younger than 2 Gyr align with the chemodynamical models of Chiappini (2009) and Minchev et al. (2013, 2014). However, for ages greater than 2 Gyr, they observed a deviation between their sample of OCs and these models.

5. Conclusions

This work shows that radial velocities and metallicities are important in classifying the star members of OCs and the likelihood of belonging. These findings highlight the correlation between radial velocity proximity and high membership probabilities. The observed pattern emphasizes the effectiveness of RV as a discriminator of membership, particularly for stars within 2σ of the mean RV. The consistency of this trend across different OCs reinforces the robustness of our membership assignment criteria, demonstrating its applicability to a wide range of clusters and providing a reliable approach for refining OC membership classifications.

The dynamic analysis of these OCs presented reveals intriguing cases of orbital dynamics, such as NGC 6705, which exhibits a chaotic configuration influenced by the Galactic bar. The banana-shaped orbit around the Lagrange points L_4 and L_5 , as well as the transient behavior around the CR , suggests a possible connection to moving groups such as the Hercules stream. These findings shed light on the dynamical influence of the bar and provide valuable insights into the origin and formation processes of stellar moving groups in the Galactic disk.

Our analysis reveals a clear distinction in metallicity gradients between younger and older OCs, which can be attributed to the formation and evolutionary history of the Galactic disk. Younger OCs, with ages below 2 Gyr, exhibit shallower gradients, reflecting a more homogeneous environment during their formation. In contrast, older OCs demonstrate steeper gradients, consistent with the extended star formation history and chemical enrichment processes that have shaped the Galactic disk. These results align with previous findings, highlighting the complex interplay of Galactic dynamics and chemical evolution in influencing the metallicity distribution of open clusters. Our study reaffirms the importance of OCs as tracers of Galactic disk evolution and provides further evidence for the significant role of age in shaping metallicity gradients.

Data availability

Full Table A.1 is available at the CDS via anonymous ftp to anonymous ftp to cdsarc.u-strasbg.fr (130.79.128.5) or via <http://cdsweb.u-strasbg.fr/cgi-bin/qcat?J/A+A/> (in preparation).

Acknowledgements. R.G. gratefully acknowledges the grant support provided by Fundação de Amparo à Pesquisa do Estado do Rio de Janeiro (FAPERJ) under the Pós-Doutorado Nota 10 (PDR-10) grant number E26-205.964/2022 and ANID Fondecyt Postdoc No. 3230001. D.S. thank the National Council for Scientific and Technological Development – CNPq process No. 404056/2021-0. J.G.F.-T. gratefully acknowledges the grants support provided by ANID Fondecyt Iniciación No. 11220340, and from the Joint Committee ESO-Government of Chile under the agreement 2023 ORP 062/2023. S.D. acknowledges CNPq/MCTI for grant 306859/2022-0 and FAPERJ for grant 210.688/2024. K.C. and V.V.S. acknowledges support from the National Science Foundation through NSF grant no. AST-2206543. V.L.-T. acknowledges a fellowship 302195/2024-6 of the PCI Program – MCTI and fellowship 152242/2024-4 of the PDJ - MCTI and CNPq.

Funding for the Sloan Digital Sky Survey IV has been provided by the Alfred P. Sloan Foundation, the U.S. Department of Energy Office of Science, and the Participating Institutions.

SDSS-IV acknowledges support and resources from the Center for High Performance Computing at the University of Utah. The SDSS website is www.sdss4.org.

SDSS-IV is managed by the Astrophysical Research Consortium for the Participating Institutions of the SDSS Collaboration including the Brazilian Participation Group, the Carnegie Institution for Science, Carnegie Mellon University, Center for Astrophysics | Harvard & Smithsonian, the Chilean Participation Group, the French Participation Group, Instituto de Astrofísica de Canarias, The Johns Hopkins University, Kavli Institute for the Physics and Mathematics of the Universe (IPMU) / University of Tokyo, the Korean Participation Group, Lawrence Berkeley National Laboratory, Leibniz Institut für Astrophysik Potsdam (AIP), Max-Planck-Institut für Astronomie (MPIA Heidelberg), Max-Planck-Institut für Astrophysik (MPA Garching), Max-Planck-Institut für Extraterrestrische Physik (MPE), National Astronomical Observatories of China, New Mexico State University, New York University, University of Notre Dame, Observatório Nacional / MCTI, The Ohio State University, Pennsylvania State University, Shanghai Astronomical Observatory, United Kingdom Participation Group, Universidad Nacional Autónoma de México, University of Arizona, University of Colorado Boulder, University of Oxford, University of Portsmouth, University of Utah, University of Virginia, University of Washington, University of Wisconsin, Vanderbilt University, and Yale University.

This work has made use of data from the European Space Agency (ESA) mission Gaia (<https://www.cosmos.esa.int/gaia>), processed by the Gaia Data Processing and Analysis Consortium (DPAC, <https://www.cosmos.esa.int/web/gaia/dpac/consortium>). Funding for the DPAC has been provided by national institutions, in particular the institutions participating in the Gaia Multilateral Agreement.

Surveys: APOGEE DR17 (Abdurro'uf et al. 2022) and Gaia EDR3 (Gaia Collaboration et al. 2021).

Softwares: Astropy (Astropy Collaboration et al. 2013), GravPot16 (<https://gravpot.ut.inam.cnrs.fr>), HDBSCAN (Campello et al. 2013), Matplotlib (Hunter 2007), mw-plot code (<https://milkyway-plot.readthedocs.io>), Numpy (Harris et al. 2020), Pandas (McKinney 2010), scikit-learn (Pedregosa et al. 2011) and Scipy (Virtanen et al. 2020).

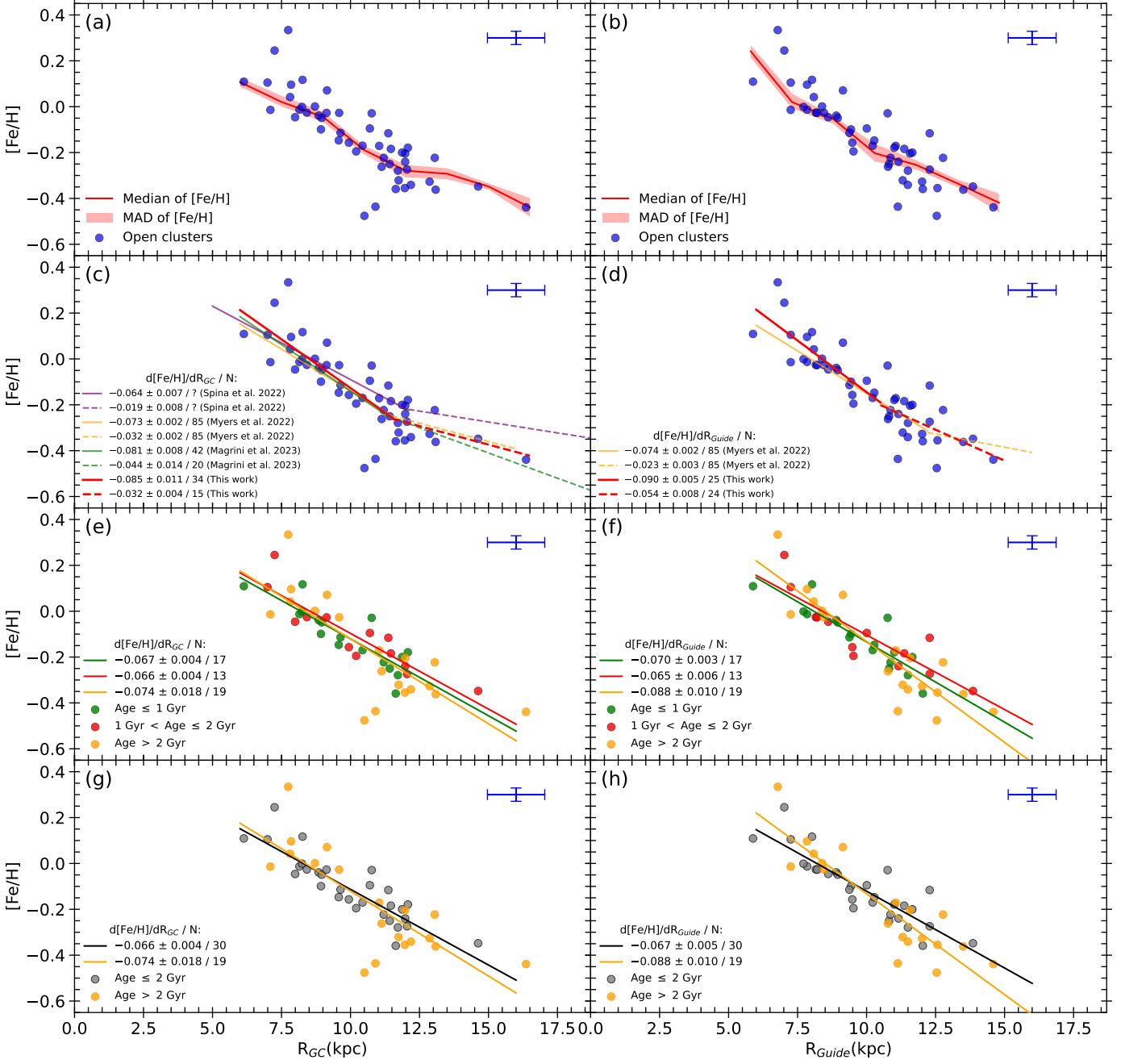


Fig. 8: Metallicity gradient, where R_{GC} is the projected Galactocentric distance and the R_{Guide} is obtained from the average between apocentre and pericentre. Blue circles represent the 49 OCs of this work. In the (a) and (b) panels, the red lines represent the median of $[\text{Fe}/\text{H}]$ for each 1.5 kpc range 6 – 16.5 kpcs (panel a) and range 6 – 15 kpcs (panel b), and the pink strip represents the median absolute deviation (MAD) of $[\text{Fe}/\text{H}]$. In the (c) and (d) panels, the red lines were obtained with two linear regressions; in (c) panel, the first in the 6 – 11.5 kpc interval (solid line) and the second in the 11.5 – 16.5 kpc interval (dashed line); in the (d) panel, the first in the 6 – 10.5 kpc interval (solid line) and the second in the 10.5 – 15 kpc interval (dashed line). In the (c) and (d) panels, we compare our results with the Spina et al. (2022) (purple lines), Myers et al. (2022) (orange lines) and Magrini et al. (2023) (green lines) results. The (e) and (f) panels separated the OCs by age: 17 OCs aged less than 1 Gyr (green circles), 13 OCs with ages between 1 and 2 Gyr (red circles), and 19 OCs aged greater than 2 Gyr (orange circles). The lines in the (e) and (f) panels are the linear regressions for each of these groups of OCs: green line (OCs aged less than 1 Gyr), red line (OCs with ages between 1 and 2 Gyr), and orange line (OCs aged greater than 2 Gyr). In panels (g) and (h), all OCs of ages under 2 Gyr are represented by gray circles, while the black line is the linear regression of these OCs. The OCs ages were obtained from Cantat-Gaudin & Anders (2020) and are aged 0.02 to 4.00 Gyr. The lines (linear regressions) this work in the panels (c), (d), (e), (f), (g), and (h) were determined with the `sklearn.linear_model` package in Python (Pedregosa et al. 2011). Ages were obtained from Cantat-Gaudin & Anders (2020).

References

- Abdurro'uf, Accetta, K., Aerts, C., et al. 2022, The Seventeenth Data Release of the Sloan Digital Sky Surveys: Complete Release of MaNGA, MaStar, and APOGEE-2 Data
- Astropy Collaboration, Robitaille, T. P., Tollerud, E. J., et al. 2013, *Astropy: A community Python package for astronomy*
- Bailer-Jones, C. A. L., Rybizki, J., Fouesneau, M., Demleitner, M., & Andrae, R. 2021, *VizieR Online Data Catalog: Distances to 1.47 billion stars in Gaia EDR3* (Bailer-Jones+, 2021), *VizieR On-line Data Catalog: I/352*. Originally published in: 2021AJ....161..147B
- Barbuy, B., Chiappini, C., & Gerhard, O. 2018, *ARA&A*, 56, 223
- Belokurov, V., Erkal, D., Evans, N. W., Koposov, S. E., & Deason, A. J. 2018, *MNRAS*, 478, 611
- Bovy, J. 2015, *ApJS*, 216, 29
- Bovy, J. 2016, *ApJ*, 817, 49
- Campello, R. J. G. B., Moulavi, D., & Sander, J. 2013, in *Advances in Knowledge Discovery and Data Mining*, ed. J. Pei, V. S. Tseng, L. Cao, H. Motoda, & G. Xu (Berlin, Heidelberg: Springer Berlin Heidelberg), 160–172
- Campello, R. J. G. B., Moulavi, D., Zimek, A., & Sander, J. 2015, *ACM Trans. Knowl. Discov. Data*, 10
- Cantat-Gaudin, T. & Anders, F. 2020, *A&A*, 633, A99
- Cantat-Gaudin, T. & Casamiquela, L. 2024, *New A Rev.*, 99, 101696
- Carollo, D., Beers, T. C., Chiba, M., et al. 2010, *ApJ*, 712, 692
- Carraro, G., Ng, Y. K., & Portinari, L. 1998, *MNRAS*, 296, 1045
- Casamiquela, L., Soubiran, C., Jofré, P., et al. 2021, *A&A*, 652, A25
- Castro-Ginard, A., Jordi, C., Luri, X., et al. 2022, *A&A*, 661, A118
- Castro-Ginard, A., Jordi, C., Luri, X., et al. 2018, *A&A*, 618, A59
- Chen, L., Hou, J. L., & Wang, J. J. 2003, *AJ*, 125, 1397
- Chi, H., Wang, F., & Li, Z. 2023, *Research in Astronomy and Astrophysics*, 23, 065008
- Chiappini, C. 2009, in *IAU Symposium, Vol. 254, The Galaxy Disk in Cosmological Context*, ed. J. Andersen, Nordströara, B. m, & J. Bland-Hawthorn, 191–196
- Dehnen, W. & Binney, J. 1998, *MNRAS*, 294, 429
- Donor, J., Frinchaboy, P. M., Cunha, K., et al. 2020, *AJ*, 159, 199
- Eilers, A.-C., Hogg, D. W., Rix, H.-W., & Ness, M. K. 2019, *ApJ*, 871, 120
- Ester, M., Kriegel, H.-P., Sander, J., & Xu, X. 1996, in *Proceedings of the Second International Conference on Knowledge Discovery and Data Mining, KDD'96* (AAAI Press), 226–231
- Fernández-Trincado, J. G. 2017, PhD thesis, Université de Franche-Comte, Besançon, France
- Fernández-Trincado, J. G., Beers, T. C., Tang, B., et al. 2019, *MNRAS*, 488, 2864
- Friel, E. D. 1995, *ARA&A*, 33, 381
- Friel, E. D., Janes, K. A., Tavares, M., et al. 2002, *AJ*, 124, 2693
- Gaia Collaboration, Brown, A. G. A., Vallenari, A., et al. 2018, *A&A*, 616, A1
- Gaia Collaboration, Brown, A. G. A., Vallenari, A., et al. 2021, *A&A*, 649, A1
- Gaia Collaboration, Prusti, T., de Bruijne, J. H. J., et al. 2016, *A&A*, 595, A1
- García Pérez, A. E., Allende Prieto, C., Holtzman, J. A., et al. 2016, *AJ*, 151, 144
- Gilmore, G., Randich, S., Asplund, M., et al. 2012, *The Messenger*, 147, 25
- GRAVITY Collaboration, Abuter, R., Amorim, A., et al. 2021, *A&A*, 647, A59
- Grilo, V., Souto, D., Cunha, K., et al. 2024, *MNRAS*[arXiv:2409.15207]
- Gunn, J. E., Siegmund, W. A., Mannery, E. J., et al. 2006, *AJ*, 131, 2332
- Harris, C. R., Millman, K. J., van der Walt, S. J., et al. 2020, *Nature*, 585, 357–362
- Hopfield, J. J. & Tank, D. W. 1986, *Science*, 233, 625
- Hunt, E. L. & Reffert, S. 2021, *A&A*, 646, A104
- Hunt, E. L. & Reffert, S. 2023, *A&A*, 673, A114
- Hunter, J. D. 2007, *Computing in Science and Engineering*, 9, 90
- Jönsson, H., Holtzman, J. A., Prieto, C. A., et al. 2020, *The Astronomical Journal*, 160, 120
- Loaiza-Tacuri, V., Cunha, K., Souto, D., et al. 2023, *MNRAS*, 526, 2378
- Magrini, L., Sestito, P., Randich, S., & Galli, D. 2009, *A&A*, 494, 95
- Magrini, L., Viscasillas Vázquez, C., Spina, L., et al. 2023, *A&A*, 669, A119
- Majewski, S. R., Schiavon, R. P., Frinchaboy, P. M., et al. 2017, *AJ*, 154, 94
- Martell, S. L., Sharma, S., Buder, S., et al. 2017, *MNRAS*, 465, 3203
- Matteucci, F. 2021, *A&A Rev.*, 29, 5
- McKinney, W. 2010, in *Proceedings of the 9th Python in Science Conference*, ed. S. van der Walt & J. Millman, 51 – 56
- McMillan, P. J. 2017a, *MNRAS*, 466, 174
- McMillan, P. J. 2017b, *MNRAS*, 465, 76
- Minchev, I., Chiappini, C., & Martig, M. 2013, *A&A*, 558, A9
- Minchev, I., Chiappini, C., & Martig, M. 2014, *A&A*, 572, A92
- Myers, N., Donor, J., Spoo, T., et al. 2022, *AJ*, 164, 85
- Netopil, M., Oralhan, İ. A., Çakmak, H., Michel, R., & Karataş, Y. 2022, *MNRAS*, 509, 421
- Nidever, D. L., Holtzman, J. A., Allende Prieto, C., et al. 2015, *AJ*, 150, 173
- Palla, M., Magrini, L., Spitoni, E., et al. 2024, *A&A*, 690, A334
- Pedregosa, F., Varoquaux, G., Gramfort, A., et al. 2011, *Journal of Machine Learning Research*, 12, 2825
- Pérez-Villegas, A., Portail, M., Wegg, C., & Gerhard, O. 2017, *ApJ*, 840, L2
- Quispe-Huaynasi, F., Roig, F., McDonald, D. J., et al. 2022, *AJ*, 164, 187
- Randich, S., Gilmore, G., Magrini, L., et al. 2022, *A&A*, 666, A121
- Robin, A. C., Marshall, D. J., Schultheis, M., & Reylé, C. 2012, *A&A*, 538, A106
- Robin, A. C., Reylé, C., Derrière, S., & Picaud, S. 2003, *A&A*, 409, 523
- Robin, A. C., Reylé, C., Fliri, J., et al. 2014, *A&A*, 569, A13
- Sanders, J. L., Smith, L., & Evans, N. W. 2019, *MNRAS*, 488, 4552
- Schiappacasse-Ulloa, J., Tang, B., Fernández-Trincado, J. G., et al. 2018, *AJ*, 156, 94
- Schönrich, R., Binney, J., & Dehnen, W. 2010, *MNRAS*, 403, 1829
- Sinha, A., Zasowski, G., Frinchaboy, P., et al. 2024, *ApJ*, 975, 89
- Soubiran, C., Cantat-Gaudin, T., Romero-Gómez, M., et al. 2018, *A&A*, 619, A155
- Spina, L., Magrini, L., & Cunha, K. 2022, *Universe*, 8, 87
- Spitoni, E., Recio-Blanco, A., de Laverny, P., et al. 2023, *A&A*, 670, A109
- Spitzer, L. 1958, *Ricerche Astronomiche*, 5, 445
- Spitzer, Jr., L. & Harm, R. 1958, *ApJ*, 127, 544
- Tang, B., Fernández-Trincado, J. G., Geisler, D., et al. 2018, *ApJ*, 855, 38
- Teuben, P. 1995, in *Astronomical Society of the Pacific Conference Series, Vol. 77, Astronomical Data Analysis Software and Systems IV*, ed. R. A. Shaw, H. E. Payne, & J. J. E. Hayes, 398
- Vasiliev, E. 2019, *MNRAS*, 482, 1525
- Virtanen, P., Gommers, R., Oliphant, T. E., et al. 2020, *Nature Methods*, 17, 261
- Wilson, J. C., Hearty, F., Skrutskie, M. F., et al. 2010, in *Society of Photo-Optical Instrumentation Engineers (SPIE) Conference Series, Vol. 7735, Ground-based and Airborne Instrumentation for Astronomy III*, ed. I. S. McLean, S. K. Ramsay, & H. Takami, 77351C
- Wilson, J. C., Hearty, F. R., Skrutskie, M. F., et al. 2019, *PASP*, 131, 055001

Appendix A: Table of the stars classified as members

Table A.1: Stars classified as members

ID*	OC**	RA[J2000] (deg)	DEC[J2000] (deg)	probability*** (%)
2MASS J05195385+3035095	Berkeley 17	79.974375	+30.585985	100
2MASS J05202118+3035544	Berkeley 17	80.088262	+30.598465	100
2MASS J05202905+3032414	Berkeley 17	80.121082	+30.544847	100
2MASS J05203121+3035067	Berkeley 17	80.130056	+30.585209	100
2MASS J05203650+3030351	Berkeley 17	80.152085	+30.509773	77.9
2MASS J05203799+3034414	Berkeley 17	80.158321	+30.578190	100
2MASS J05204143+3036042	Berkeley 17	80.172651	+30.601170	90.9
2MASS J05204488+3038020	Berkeley 17	80.187027	+30.633909	100
2MASS J05211671+4533170	Berkeley 18	80.319637	+45.554745	88.5
2MASS J05211693+4524226	Berkeley 18	80.320575	+45.406296	5.84
2MASS J05214903+4548331	Berkeley 18	80.454298	+45.809196	16.8
2MASS J05214927+4525225	Berkeley 18	80.455304	+45.422939	100
2MASS J05215476+4526226	Berkeley 18	80.478189	+45.439617	79.7
2MASS J05215704+4521220	Berkeley 18	80.487685	+45.356113	100
2MASS J05220382+4530273	Berkeley 18	80.515940	+45.507591	70.9
2MASS J05220607+4520585	Berkeley 18	80.525311	+45.349609	100
2MASS J05220733+4524235	Berkeley 18	80.530573	+45.406536	48.7
2MASS J05220741+4525388	Berkeley 18	80.530896	+45.427448	47.4
2MASS J05221065+4528494	Berkeley 18	80.544413	+45.480389	47.7
2MASS J05221114+4517206	Berkeley 18	80.546446	+45.289062	100
2MASS J05221426+4527000	Berkeley 18	80.559428	+45.450027	13.7
2MASS J05221711+4523410	Berkeley 18	80.571305	+45.394733	25.4
2MASS J05221874+4525191	Berkeley 18	80.578115	+45.421982	100
2MASS J05221919+4529451	Berkeley 18	80.579991	+45.495884	47.7
2MASS J05222163+4531589	Berkeley 18	80.590152	+45.533039	100
2MASS J05222297+4518588	Berkeley 18	80.595725	+45.316360	100
2MASS J05222413+4522021	Berkeley 18	80.600544	+45.367256	100
2MASS J05222556+4525370	Berkeley 18	80.606519	+45.426964	45.4
2MASS J05222722+4520061	Berkeley 18	80.613418	+45.335052	46.6
2MASS J05222848+4523173	Berkeley 18	80.618708	+45.388153	100
2MASS J05222878+4527249	Berkeley 18	80.619922	+45.456917	96.7
2MASS J05223463+4531085	Berkeley 18	80.644327	+45.519051	100
2MASS J05223696+4524397	Berkeley 18	80.654019	+45.411034	100
2MASS J05223884+4520031	Berkeley 18	80.661871	+45.334213	47.4
2MASS J05224064+4523367	Berkeley 18	80.669348	+45.393555	100
2MASS J05224234+4459401	Berkeley 18	80.676453	+44.994488	36.2
2MASS J05225704+4529067	Berkeley 18	80.737684	+45.485218	100
2MASS J05230111+4526218	Berkeley 18	80.754631	+45.439396	100
2MASS J05230556+4522198	Berkeley 18	80.773168	+45.372177	56.7
...
2MASS J12400260-6039545	Trumpler 20	190.01086	-60.665142	100
2MASS J12400451-6036566	Trumpler 20	190.01879	-60.615726	100
2MASS J12400755-6035445	Trumpler 20	190.03148	-60.595695	100
2MASS J12402228-6037419	Trumpler 20	190.09286	-60.628311	100
2MASS J12402480-6043101	Trumpler 20	190.10335	-60.719498	100
2MASS J12402949-6038518	Trumpler 20	190.12290	-60.647732	100

Notes: The full list of 1987 stars is available in the CDS database (Vizier; in preparation). * The ID column identifies the member stars with their 2MASS names. ** The OC column identifies the OC to which the star was classified as a member. *** In the last column is the probability of star belonging to the OC using HDBSCAN.

Appendix B: Open cluster tables

Table B.1: Parameters used in HDBSCAN

OC	N_{all}	$N_{>50\%}$	$N_{>80\%}$	$\langle RA \rangle^*$ ($^{\circ}$)	$\langle DEC \rangle^*$ ($^{\circ}$)	$\langle \mu_{RA} \rangle^*$ (mas/yr)	$\langle \mu_{DEC} \rangle^*$ (mas/yr)	$\langle \pi \rangle^*$ (mas)	$\langle RV \rangle^*$ (km/s)	$\langle [Fe/H] \rangle^*$ (dex)	$m_{c, size}$	age** (Gyr)
Berkeley 17	8	8	7	+80.1[0.07]	+30.6[0.03]	+2.53[0.04]	-0.39[0.07]	0.30[0.02]	-73.4[0.27]	-0.17[0.03]	6	7.24
Berkeley 18	31	19	16	+80.6[0.10]	+45.4[0.07]	+0.76[0.05]	-0.09[0.05]	0.16[0.03]	-2.58[0.33]	-0.36[0.03]	3	4.37
Berkeley 19	6	5	3	+81.0[0.03]	+29.8[0.29]	+0.48[0.23]	-0.10[0.18]	0.26[0.13]	+18.1[0.57]	-0.36[0.02]	2	2.19
Berkeley 20	11	9	4	+83.2[0.05]	+0.19[0.01]	+0.79[0.15]	-0.30[0.07]	0.06[0.04]	+78.6[2.00]	-0.44[0.06]	3	4.79
Berkeley 21	10	8	8	+88.0[0.06]	+21.8[0.14]	+0.50[0.09]	-0.82[0.53]	0.16[0.05]	+0.84[0.55]	-0.22[0.04]	6	2.14
Berkeley 22	9	5	3	+89.6[0.05]	+7.76[0.03]	+0.61[0.01]	-0.37[0.02]	0.15[0.04]	+95.3[0.13]	-0.33[0.02]	3	2.45
Berkeley 33	18	9	4	+104.0[0.05]	-13.0[0.29]	-0.79[0.17]	+1.47[0.23]	0.19[0.03]	+78.2[0.34]	-0.28[0.04]	3	0.23
Berkeley 53	14	8	5	+314.0[0.04]	+51.1[0.04]	-3.83[0.09]	-5.69[0.04]	0.23[0.03]	-36.2[0.47]	-0.10[0.03]	4	0.98
Berkeley 66	11	7	6	+46.1[0.04]	+58.8[0.02]	-0.17[0.07]	+0.07[0.05]	0.18[0.06]	-50.0[0.23]	-0.20[0.02]	2	3.09
Berkeley 71	10	4	4	+85.2[0.02]	+32.3[0.02]	+0.65[0.03]	-1.67[0.01]	0.26[0.04]	-9.44[0.12]	-0.25[0.02]	3	0.87
Berkeley 98	4	3	3	+341.0[4.4]	+52.6[0.14]	-1.32[0.01]	-3.23[0.06]	0.25[0.01]	-69.1[0.26]	-0.03[0.02]	2	2.45
Collinder 261	8	5	4	+190.0[0.05]	-68.4[0.02]	-6.42[0.08]	-2.63[0.04]	0.35[0.01]	-25.2[0.08]	-0.01[0.01]	3	6.31
Czemik 20	20	12	7	+80.0[0.25]	+39.4[0.27]	+0.44[0.22]	-1.60[0.25]	0.27[0.06]	+30.8[0.77]	-0.18[0.03]	5	1.66
Czemik 21	4	4	3	+81.7[0.07]	+36.1[0.06]	+2.18[0.13]	-1.01[0.08]	0.24[0.02]	+45.5[0.57]	-0.32[0.00]	2	2.57
FSR2007 0494	6	3	3	+64.3[0.05]	+63.8[0.02]	-2.49[0.04]	-0.93[0.03]	0.21[0.02]	-64.7[0.16]	-0.03[0.01]	2	0.89
IC 166	25	9	7	+28.1[0.09]	+61.8[0.05]	-1.46[0.05]	+1.05[0.04]	0.22[0.07]	-39.8[0.19]	-0.12[0.03]	5	1.32
IC 1369	7	3	3	+318.0[0.04]	+47.8[0.01]	-4.56[0.02]	-5.70[0.07]	0.27[0.02]	-48.7[0.09]	-0.04[0.03]	2	0.29
King 5	16	15	3	+48.7[0.14]	+52.7[0.04]	-0.29[0.16]	-1.32[0.04]	0.43[0.02]	-43.8[0.70]	-0.16[0.02]	2	1.02
King 7	7	5	4	+59.8[0.04]	+51.8[0.02]	+0.99[0.07]	-1.17[0.04]	0.37[0.04]	-10.4[0.16]	-0.17[0.02]	2	0.22
King 8	5	3	3	+87.2[0.25]	+33.8[0.18]	+0.35[0.08]	-2.15[0.43]	0.18[0.06]	-1.12[0.17]	-0.18[0.05]	2	0.83
M 35	101	76	32	+92.3[0.15]	+24.4[0.17]	+2.23[0.13]	-2.80[0.13]	1.15[0.03]	-7.42[0.42]	-0.05[0.04]	6	0.15
M 44	185	143	69	+129.0[4.6]	+19.6[0.41]	-35.8[0.56]	-12.9[0.48]	5.42[0.07]	+35.3[0.51]	+0.12[0.07]	10	0.68
M 67	378	328	257	+133.0[1.7]	+11.8[0.19]	-11.0[0.15]	-2.92[0.16]	1.15[0.05]	+34.2[0.57]	+0.00[0.06]	5	4.27
Melotte 71	7	6	4	+114.0[0.03]	-12.1[0.03]	-2.41[0.09]	+4.26[0.20]	0.49[0.07]	+51.0[0.39]	-0.15[0.02]	2	0.98
NGC 188	69	45	39	+12.0[1.28]	+85.2[0.16]	-2.34[0.10]	-1.04[0.07]	0.52[0.02]	-41.8[0.63]	+0.07[0.04]	3	7.08
NGC 752	105	76	35	+29.3[0.28]	+37.8[0.19]	+9.76[0.18]	-11.8[0.19]	2.26[0.05]	+6.21[0.41]	-0.03[0.05]	6	1.17
NGC 1193	9	4	4	+46.6[0.03]	+44.4[0.02]	-0.24[0.05]	-0.43[0.04]	0.18[0.03]	-84.8[0.24]	-0.34[0.02]	3	5.13
NGC 1245	28	22	20	+48.7[0.10]	+47.3[0.06]	+0.47[0.07]	-1.67[0.04]	0.30[0.02]	-29.4[0.43]	-0.10[0.02]	5	1.20
NGC 1798	9	7	7	+77.9[0.03]	+47.7[0.02]	+0.76[0.07]	-0.37[0.04]	0.21[0.03]	+2.73[0.58]	-0.27[0.03]	2	1.66
NGC 1857	5	5	3	+80.0[0.28]	+39.7[0.24]	+0.38[0.17]	-1.55[0.27]	0.31[0.10]	+1.38[0.17]	-0.22[0.06]	2	0.25
NGC 1907	4	3	3	+82.0[0.04]	+35.3[0.01]	-0.18[0.04]	-3.45[0.07]	0.64[0.04]	+2.68[0.16]	-0.11[0.01]	2	0.59
NGC 2158	58	57	56	+91.9[0.06]	+24.1[0.08]	-0.23[0.09]	-1.99[0.07]	0.23[0.05]	+27.2[1.24]	-0.24[0.03]	3	1.55
NGC 2204	24	16	9	+93.8[0.10]	-18.6[0.06]	-0.58[0.04]	+1.95[0.04]	0.22[0.02]	+92.2[0.11]	-0.26[0.04]	5	2.09
NGC 2243	15	13	13	+97.4[0.07]	-31.3[0.10]	-1.24[0.04]	+5.50[0.04]	0.22[0.01]	+60.0[0.45]	-0.48[0.04]	2	4.37
NGC 2324	8	4	4	+106.0[0.03]	+1.05[0.06]	-0.36[0.02]	-0.05[0.05]	0.22[0.01]	+72.4[0.18]	-0.20[0.02]	3	0.54
NGC 2420	19	19	16	+115.0[0.03]	+21.6[0.05]	-1.25[0.04]	-1.99[0.07]	0.41[0.02]	+44.4[0.30]	-0.20[0.02]	2	1.74
NGC 4337	12	7	4	+186.0[0.03]	-58.1[0.02]	-8.82[0.08]	+1.55[0.03]	0.38[0.01]	-17.7[0.16]	+0.25[0.04]	3	1.45
NGC 6705	20	7	6	+283.0[0.02]	-6.27[0.04]	-1.49[0.11]	-4.20[0.11]	0.41[0.03]	+34.8[0.20]	+0.11[0.04]	3	0.31

Notes: N_{all} , $N_{>50\%}$ and $N_{>80\%}$ are the number of stars considering all probabilities, probabilities above 50 % and probabilities above 80 %, respectively. * Average values obtained with the stars member with probabilities greater than 80 %. The values that are between brackets are standard deviations. The $m_{c, size}$ were chosen based on the minor standard deviation of $\langle [Fe/H] \rangle$. ** Ages from Cantat-Gaudin & Anders (2020).

Table B.1: Parameters used in HDBSCAN (continued)

OC	N_{all}	$N_{>50\%}$	$N_{>80\%}$	$\langle RA \rangle^*$ ($^{\circ}$)	$\langle DEC \rangle^*$ ($^{\circ}$)	$\langle \mu_{RA} \rangle^*$ (mas/yr)	$\langle \mu_{DEC} \rangle^*$ (mas/yr)	$\langle \pi \rangle^*$ (mas)	$\langle RV \rangle^*$ (km/s)	$\langle [Fe/H] \rangle^*$ (dex)	$m_{c, size}$	age** (Gyr)
NGC 6791	79	64	47	+290.[0.08]	+37.8[0.08]	-0.39[0.06]	-2.25[0.06]	0.21[0.02]	-47.2[0.77]	+0.33[0.04]	6	6.31
NGC 6811	11	6	3	+294.[0.07]	+46.5[0.06]	-3.29[0.06]	-8.83[0.06]	0.89[0.00]	+7.40[0.06]	-0.05[0.01]	2	1.07
NGC 6819	79	39	19	+295.[0.05]	+40.2[0.06]	-2.85[0.10]	-3.94[0.07]	0.38[0.02]	+2.76[0.38]	+0.04[0.03]	5	2.24
NGC 7058	7	6	5	+321.[0.19]	+50.9[0.07]	+7.40[0.18]	+2.96[0.37]	2.73[0.02]	-19.2[0.21]	-0.01[0.03]	4	0.04
NGC 7789	95	62	49	+359.[0.16]	+56.8[0.10]	-0.94[0.11]	-2.02[0.10]	0.50[0.02]	-54.4[0.71]	-0.03[0.03]	5	1.55
Pleiades	306	223	86	+56.5[0.59]	+24.1[0.63]	+20.0[0.69]	-45.5[0.71]	7.38[0.10]	+5.95[0.60]	-0.00[0.06]	5	0.08
Ruprecht 147	59	30	16	+289.[0.26]	-16.3[0.20]	-0.80[0.31]	-26.8[0.28]	3.28[0.03]	+42.2[0.28]	+0.10[0.02]	3	3.02
Teutsch 51	10	5	2	+88.5[0.03]	+26.8[0.01]	+0.56[0.05]	-0.22[0.10]	0.24[0.03]	+17.7[0.20]	-0.36[0.01]	2	0.68
Tombaugh 2	17	9	5	+106.[0.02]	-20.8[0.02]	-0.51[0.04]	+1.47[0.08]	0.07[0.07]	+121.[0.34]	-0.35[0.02]	4	1.62
Trumpler 5	12	5	5	+99.3[0.11]	+9.54[0.15]	-0.65[0.08]	+0.24[0.07]	0.30[0.01]	+50.5[0.42]	-0.44[0.02]	3	4.27
Trumpler 20	26	25	23	+190.[0.11]	-60.6[0.05]	-7.08[0.07]	+0.16[0.11]	0.27[0.02]	-40.1[0.47]	+0.11[0.02]	2	1.86

Notes: N_{all} , $N_{>50\%}$ and $N_{>80\%}$ are the number of stars considering all probabilities, probabilities above 50 % and probabilities above 80 %, respectively. * Average values obtained with the stars member with probabilities greater than 80 %. The values that are between brackets are standard deviations. The $m_{c, size}$ were chosen based on the minor standard deviation of $\langle [Fe/H] \rangle$. ** Ages from Cantat-Gaudin & Anders (2020).

Table B.2: Galactocentric positions and dynamic properties of OCs

OC	X (kpc)	Y (kpc)	Z (kpc)	R_{GC} (kpc)	V_R ($\text{km}\cdot\text{s}^{-1}$)	V_{ϕ} ($\text{km}\cdot\text{s}^{-1}$)	e	Z_{max} (kpc)	pericentre (kpc)	apocentre (kpc)	R_{Guide} (kpc)
Berkeley 17	10.91	-0.222	-0.188	11.04	-76.02	228.5	0.239±0.001	1.578±0.105	8.412±0.106	13.70±0.168	11.05±0.273
Berkeley 18	12.89	-1.435	+0.450	13.09	+15.75	243.8	0.065±0.007	1.039±0.259	12.63±0.683	14.38±0.971	13.50±1.654
Berkeley 19	11.84	-0.220	-0.235	11.97	+12.33	251.1	0.073±0.013	0.506±0.233	11.68±1.188	13.46±1.517	12.57±2.705
Berkeley 20	15.87	+3.419	-2.684	16.36	+10.17	205.9	0.130±0.025	2.769±0.846	12.70±1.353	16.49±2.274	14.59±3.627
Berkeley 21	12.92	+0.593	-0.216	13.05	-23.69	233.4	0.083±0.017	0.371±0.201	11.64±0.919	13.90±1.045	12.77±1.964
Berkeley 22	12.63	+1.674	-0.700	12.87	+45.47	218.3	0.166±0.005	0.831±0.094	10.02±0.516	14.01±0.569	12.01±1.085
Berkeley 33	11.15	+3.182	-0.358	11.72	+4.108	236.6	0.028±0.014	0.379±0.042	11.23±0.625	11.76±0.412	11.50±1.037
Berkeley 53	8.020	-3.668	+0.240	8.929	-25.84	256.1	0.100±0.036	0.329±0.080	8.496±0.222	10.38±1.118	9.437±1.340
Berkeley 66	11.48	-2.983	+0.016	11.98	+7.051	233.0	0.038±0.014	0.198±0.045	11.20±0.886	11.96±1.100	11.58±1.986
Berkeley 71	11.30	-0.194	+0.050	11.42	-14.89	228.9	0.064±0.008	0.075±0.010	10.12±0.171	11.51±0.378	10.82±0.550
Berkeley 98	8.850	-3.380	-0.342	9.588	+3.104	210.2	0.145±0.005	0.688±0.068	7.234±0.127	9.681±0.080	8.458±0.207
Collinder 261	6.605	+2.261	-0.257	7.097	-9.867	249.7	0.061±0.002	0.537±0.020	6.812±0.032	7.689±0.034	7.251±0.066
Czernik 20	11.32	-0.685	+0.073	11.46	+38.67	236.6	0.124±0.009	0.118±0.063	9.937±0.335	12.80±0.567	11.37±0.902
Czernik 21	11.61	-0.516	+0.032	11.74	+48.81	226.1	0.161±0.006	1.235±0.149	9.481±0.126	13.14±0.256	11.31±0.382
FSR2007 0494	10.05	-3.535	+0.073	10.77	-6.635	241.9	0.031±0.004	0.195±0.030	10.45±0.311	11.07±0.290	10.76±0.602
IC 166	10.76	-3.287	-0.014	11.37	+12.59	255.5	0.093±0.047	0.755±0.385	11.18±1.066	13.39±2.651	12.29±3.717
IC 1369	7.974	-3.570	-0.025	8.848	-37.53	243.7	0.118±0.007	0.054±0.027	7.861±0.327	9.944±0.554	8.902±0.881
King 5	9.736	-1.272	-0.159	9.940	-14.62	230.5	0.091±0.002	0.179±0.011	8.623±0.071	10.34±0.089	9.483±0.159
King 7	10.23	-1.299	-0.045	10.43	+18.93	234.9	0.084±0.018	0.120±0.014	9.379±0.068	11.06±0.376	10.22±0.443
King 8	11.95	-0.262	+0.210	12.08	-4.102	218.8	0.085±0.035	0.323±0.140	10.03±0.619	11.98±0.470	11.00±1.089
M 35	8.834	+0.097	+0.034	8.956	-22.84	243.4	0.080±0.001	0.190±0.011	8.234±0.020	9.675±0.022	8.955±0.042

Table B.2: Galactocentric positions and dynamic properties of OCs (continued)

OC	X (kpc)	Y (kpc)	Z (kpc)	R_{GC} (kpc)	V_R ($\text{km}\cdot\text{s}^{-1}$)	V_ϕ ($\text{km}\cdot\text{s}^{-1}$)	e	Z_{max} (kpc)	pericentre (kpc)	apocentre (kpc)	R_{Guide} (kpc)
M 44	8.140	+0.067	+0.096	8.262	+29.82	236.8	0.099±0.004	0.110±0.004	7.229±0.020	8.817±0.097	8.023±0.118
M 67	8.581	+0.417	+0.445	8.772	+24.89	233.8	0.086±0.002	0.557±0.041	7.663±0.032	9.110±0.046	8.387±0.078
Melotte 71	9.329	+1.527	+0.160	9.573	+16.81	255.4	0.107±0.027	0.323±0.040	9.104±0.279	11.45±0.682	10.28±0.961
NGC 188	8.917	-1.420	+0.695	9.148	-9.340	242.6	0.045±0.003	0.847±0.028	8.730±0.070	9.556±0.066	9.143±0.136
NGC 752	8.293	-0.273	-0.172	8.420	+13.47	236.4	0.060±0.002	0.273±0.005	7.675±0.021	8.648±0.009	8.161±0.030
NGC 1193	11.81	-2.487	-0.978	12.19	-37.28	222.5	0.136±0.008	1.183±0.038	9.936±0.442	13.05±0.373	11.49±0.815
NGC 1245	10.46	-1.617	-0.461	10.70	+7.018	225.8	0.067±0.011	0.477±0.019	9.333±0.150	10.68±0.110	10.01±0.260
NGC 1798	11.85	-1.348	+0.346	12.05	+23.22	242.6	0.080±0.005	0.676±0.060	11.31±0.220	13.27±0.375	12.29±0.594
NGC 1857	11.06	-0.643	+0.078	11.20	+8.661	235.4	0.044±0.019	0.106±0.056	10.40±0.571	11.33±0.704	10.87±1.275
NGC 1907	9.514	-0.196	+0.008	9.638	-0.890	237.3	0.043±0.004	0.161±0.019	8.972±0.027	9.784±0.083	9.378±0.111
NGC 2158	11.85	+0.448	+0.121	11.98	+4.670	224.1	0.065±0.018	0.446±0.239	10.42±0.317	11.89±0.773	11.16±1.090
NGC 2204	10.66	+2.751	-1.107	11.13	+21.66	231.4	0.087±0.010	1.228±0.062	9.835±0.281	11.72±0.116	10.78±0.397
NGC 2243	9.882	+3.192	-1.207	10.50	+25.12	276.9	0.184±0.016	1.805±0.146	10.23±0.149	14.85±0.717	12.54±0.865
NGC 2324	11.52	+2.322	+0.241	11.87	-21.14	235.7	0.066±0.009	0.277±0.023	10.89±0.275	12.43±0.526	11.66±0.801
NGC 2420	10.06	+0.674	+0.774	10.20	+42.75	221.9	0.158±0.002	0.905±0.029	8.019±0.053	11.03±0.076	9.524±0.129
NGC 4337	6.810	+2.120	+0.194	7.249	+17.87	238.1	0.069±0.004	0.273±0.008	6.536±0.056	7.501±0.022	7.019±0.078
NGC 6705	5.919	-1.075	-0.115	6.136	-22.31	236.7	0.137±0.045	0.124±0.007	4.679±0.514	7.090±0.507	5.885±1.021
NGC 6791	6.593	-3.858	+0.792	7.742	+69.41	191.8	0.294±0.010	1.060±0.085	4.784±0.055	8.777±0.104	6.781±0.158
NGC 6811	7.801	-1.051	+0.229	7.992	-25.67	261.7	0.113±0.001	0.279±0.002	7.635±0.005	9.587±0.010	8.611±0.015
NGC 6819	7.304	-2.426	+0.378	7.812	+12.21	251.2	0.063±0.003	0.500±0.022	7.576±0.017	8.600±0.045	8.088±0.062
NGC 7058	8.019	-0.361	+0.004	8.149	+11.16	236.7	0.050±0.001	0.027±0.007	7.452±0.015	8.241±0.008	7.846±0.023
NGC 7789	8.839	-1.758	-0.182	9.133	-4.104	216.8	0.122±0.003	0.202±0.017	7.208±0.077	9.211±0.052	8.209±0.129
Pleiades	8.120	-0.029	-0.054	8.242	-3.245	228.6	0.076±0.003	0.126±0.008	7.132±0.037	8.297±0.005	7.714±0.043
Ruprecht 147	7.725	-0.105	-0.066	7.848	-55.90	238.1	0.173±0.001	0.318±0.010	6.485±0.018	9.197±0.024	7.841±0.042
Teutsch 51	11.52	+0.169	+0.029	11.64	+2.474	248.1	0.046±0.007	0.436±0.064	11.49±0.370	12.58±0.404	12.04±0.774
Tombaugh 2	12.96	+6.539	-0.986	14.62	+10.10	225.2	0.087±0.073	0.993±0.426	13.08±4.105	14.63±3.371	13.86±7.475
Trumpler 5	10.72	+1.145	+0.060	10.90	+12.28	246.4	0.053±0.003	0.080±0.016	10.55±0.117	11.72±0.139	11.13±0.255
Trumpler 20	6.281	+2.808	+0.128	6.991	-0.052	255.3	0.068±0.002	0.144±0.010	6.755±0.046	7.750±0.076	7.252±0.122

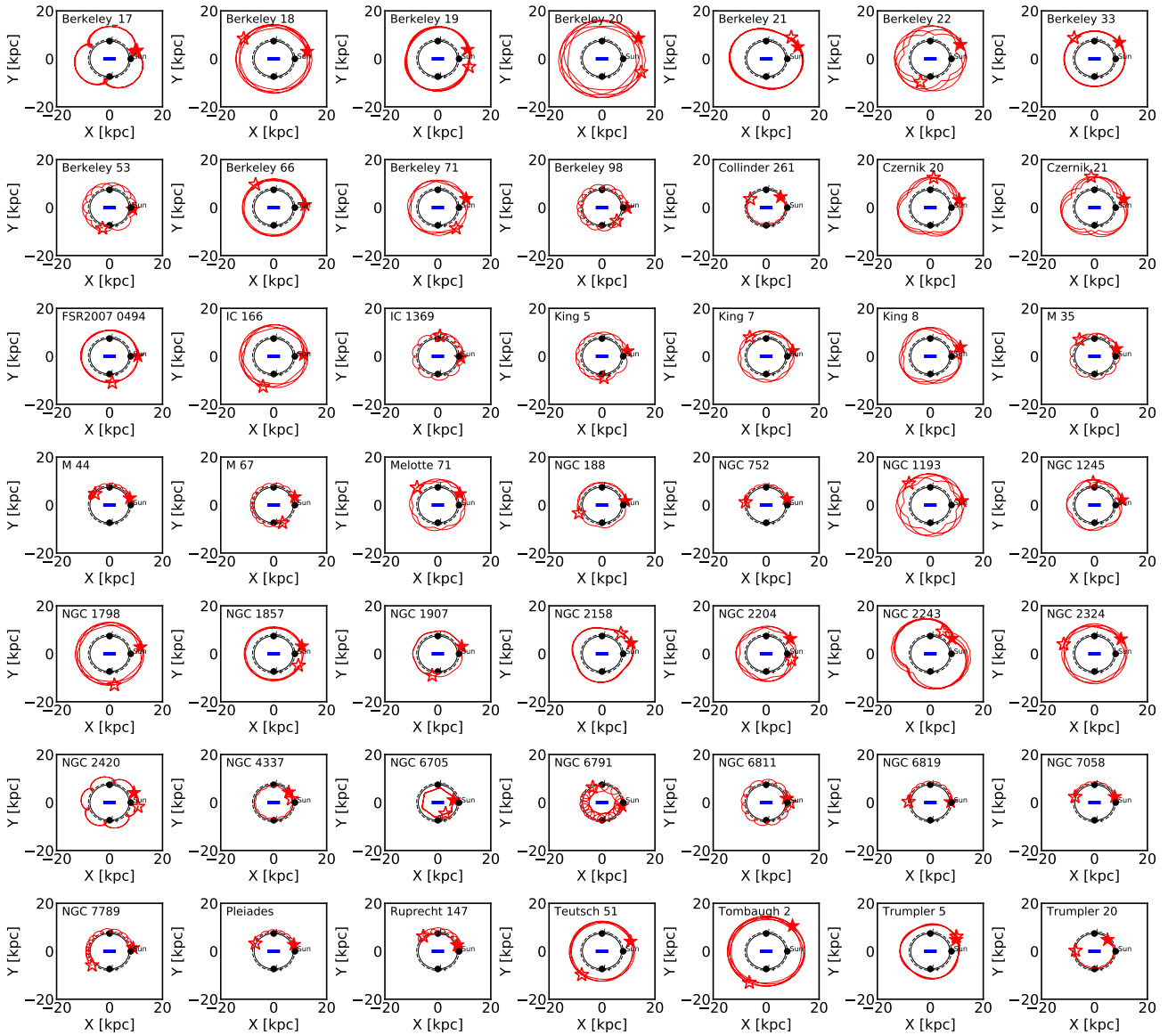
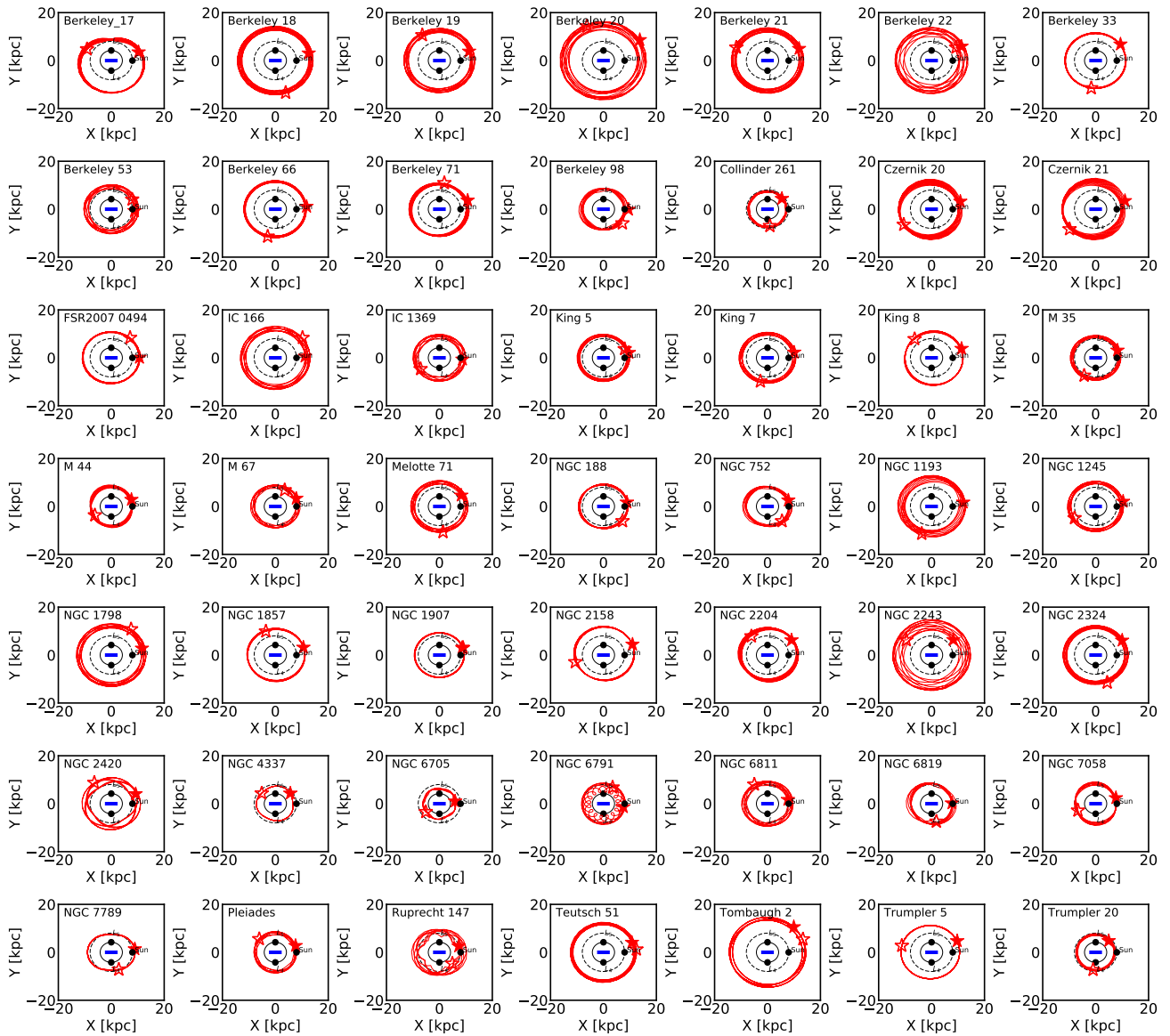
Appendix C: Orbits (adopting a bar pattern speed of $31 \text{ km s}^{-1} \text{ kpc}^{-1}$)

Fig. C.1: Orbits for the sample of selected OCs. Representative orbits projected on the equatorial Galactic plane in the non-inertial frame with a bar pattern speed of $31 \text{ km s}^{-1} \text{ kpc}^{-1}$, and time-integrated backward over 2 Gyr. The solid and dashed circles show the locations of the CR and Solar orbit, respectively, while the black dots mark the positions of the Lagrange points of the Galactic bar, L_4 and L_5 , and the current Sun position, respectively. The horizontal blue solid line shows the extension of the bar in our model (see text). The red solid line shows the orbits of the selected OCs from the observables without error bars. The red filled and unfilled star symbols indicate the initial and final positions of the OCs in our simulations, respectively.

Appendix D: Orbits (adopting a bar pattern speed of $41 \text{ km s}^{-1} \text{ kpc}^{-1}$)Fig. D.1: Same as figure C.1, results are shown here by adopting a bar pattern speed of $41 \text{ km s}^{-1} \text{ kpc}^{-1}$.

Appendix E: Orbits (adopting a bar pattern speed of $51 \text{ km s}^{-1} \text{ kpc}^{-1}$)Fig. E.1: Same as figure C.1, results are shown here by adopting a bar pattern speed of $51 \text{ km s}^{-1} \text{ kpc}^{-1}$.